Effect of Applied Resonant Magnetic Fields on the Measured MHD Mode Structure in a Tokamak Plasma

Qingjun Xiao

Submitted in partial fulfillment of the
requirements for the degree
of Doctor of Philosophy
in the Graduate School of Arts and Sciences

COLUMBIA UNIVERSITY

1998

Table of Contents

ABSTRACT

The mode structure of the m = 2 magnetohydrodynamic (MHD) instabilities has been measured in kink stabilized discharges and in the applied resonant magnetic field discharges on the High Beta Tokamak-Extended Pulse(HBT-EP). Soft X-ray signals as well as magnetic signals have been used to measure the MHD mode structures.

Plasma discharges that are kink-mode stabilized by the conducting walls are prepared for the experiments. Oscillating components of the soft X-ray signals of the detector channels located at the same radial position but different poloidal positions show a dominant poloidal mode number of m = 2. Soft X-ray radiation tomography reconstructions show m = 2 island structures which indicates that it is tearing mode.

A set of modular saddle coils producing m/n = 2/1 radial magnetic field has been installed on the HBT-EP. By selecting the oscillating current in the saddle coils, the frequency and amplitude of the applied resonant magnetic field can be programmed.

Experiments demonstrated that applied oscillating resonant magnetic fields with both single-phase and two-phase are capable of modulating the MHD mode rotation. Controlled acceleration and deceleration have been observed by programming frequency of the applied saddle coil current. The phase difference between the mode structure seen by soft X-ray tomography system and the mode structure seen by the shell mounted probes is a constant as a function of time in both the controlled acceleration and deceleration discharges. The perturbations of the soft X-ray signals from the detectors located at the same radial position but different poloidal angles clearly show we successfully controlled the rotation of m = 2 mode. Tomographic reconstruction also

identifies this mode has m = 2 island structure. It was also observed that two-phase applied perturbations induced less instantaneous modulation of the mode rotation.

Chapter 1

Introduction

This thesis will describe the mode structure measurement of the MHD instabilities during kink stabilized discharges and applied resonant magnetic field experiments on the HBT-EP tokamak. In this chapter, I will put the significance of this project in the context of nuclear fusion research, and describe briefly the project.

1.1 Energy and controlled nuclear fusion research

Human civilization and its progress depend on energy. A combination of a growing world population and expanding energy needs will exhaust oil and natural gases in the next century. Energy from nuclear fission, as an alternative source, presents a serious problem of radioactive waste disposal. Scientists and engineers, are searching for new sources of power. Controlled nuclear fusion has the virtues of potentially unlimited supply and greatly reduced amount of radioactive waste.

Nuclear reactions of interest for fusion reactors are as follows[1]:

(1) D + D –> T(1.01MeV) + p(3.03 MeV)

(2) D + D -> He^3(0.82 MeV) + n(2.45 MeV)

(3) D + T -> He^4(3.52 MeV) + n(14.06 MeV)

(4) Li^6 + n -> T + He^4 + 4.8 MeV

(5) Li^7 + n -> T + He^4 + n - 2.5 MeV

In order for nuclear fusion to occur, ions should have high relative velocities to overcome their mutual Coulomb repulsion forces. The fusion fuels are in high temperature plasma state. Hot plasmas must be enclosed long enough so that fusion reactions can take place between the ions. Ordinary containers are not suitable as they could either melt from the very hot plasma or else cool the plasma below the temperature required for nuclear fusion. One technique of containing plasma is the method of magnetic confinement. The plasma is insulateded from the walls of its container by means of a magnetic field. The most successful approach to controlled nuclear fusion to date is the tokamak.

1.2 Tokamak[2, 3]

Fig 1.1 shows a schematic of the essential components of a tokamak as well as plasma geometry.

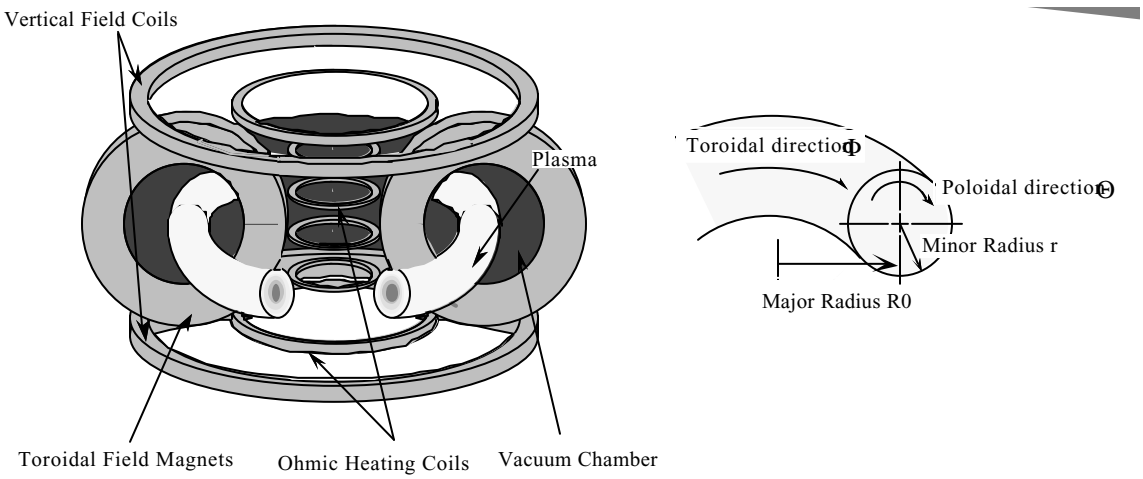

Fig 1.1 Schematic of a tokamak

A strong toroidal magnetic field is generated by the toroidal field system, creating a closed magnetic configuration necessary. Toroidal field alone is not sufficient for proper confinement. Particle vertical drifts occur because the toroidal field is stronger on the inside of the tokamak since the field lines are bent. The donut shapped toroidal vacuum chamber is filled with Hydrogen or its isotopes under low pressure. This gas when ionized, together with the ohmic heating coils, form a transformer system with the primary windings being the ohmic heating coils and the gas acting as the secondary. When current is driven through the primary winding, an inductive electric field is produced inside and its direction is along the vacuum chamber. When this field is high enough, a gaseous break-down occurs, a closed plasma ring is formed and a plasma current starts flowing toroidally within it. The current heats the plasma to high temperatures through Ohmic effect and generates a poloidal magnetic field that encloses it. This field combined with the toroidal field creates helical magnetic field lines that confine the plasma particles, eliminating the charge separation caused by the vertical magnetic drift. Finally, a magnetic field in vertical direction is applied. It interacts with the current in the plasma creating a force that counters the outward expansion of the plasma in the major radius direction. This expansion comes from two forces. One is caused by the kinetic pressure of the plasma due to the curvature of the system and the other results from the interaction of the toroidal plasma current and the poloidal field. This latter force is also known as the hoop force.

Several large tokamaks with additional heating sources were developed throughout the 1970's and 1980's, and they were equipped with advanced diagnostic systems for plasma parameters measurements. The initial physical principle of a tokamak

was simple: a plasma ring with a toroidal current immersed in a strong magnetic confining configuration. However, plasma instabilities including magnetohydrodynamic(MHD) instabilities have slowed down the development of controlled thermonuclear fusion using tokamak devices. Tokamak performance in high β discharges is often limited by long wave length kink instabilities. Here β is defined as the plasma pressure devided by magnetic pressure, i.e., $\frac{2\mu_0 p}{B^2}$. The High beta Tokamak-Extended Pulse (HBT-EP) experiment was designed to investigate the feasibility of a stable, high-ß tokamak.

1.3 HBT-EP[4, 5, 6, 7, 8]

HBT-EP tokamak was built to study MHD instabilities during high β discharges. It has a major radius 92 cm, and a minor radius 14 - 19.3 cm. The plasma current is usually less than 25 kA. The machine usually runs with a pulse length less than 10 ms. The toroidal field is about 3 kG. The line integrated plasma temperature is about 100 eV. The plasma density is 1 x 10^{13} cm^{-3}.

One of the unique features of HBT-EP is an movable conducting shell(see Figure 1.2). It consists of 20 segments located at 10 toroidal locations, two in each of the ten vacuum chamber portions. Each segment is attached to a shell positioner, so the distance between the shell and the plasma can be manually adjusted between shots.

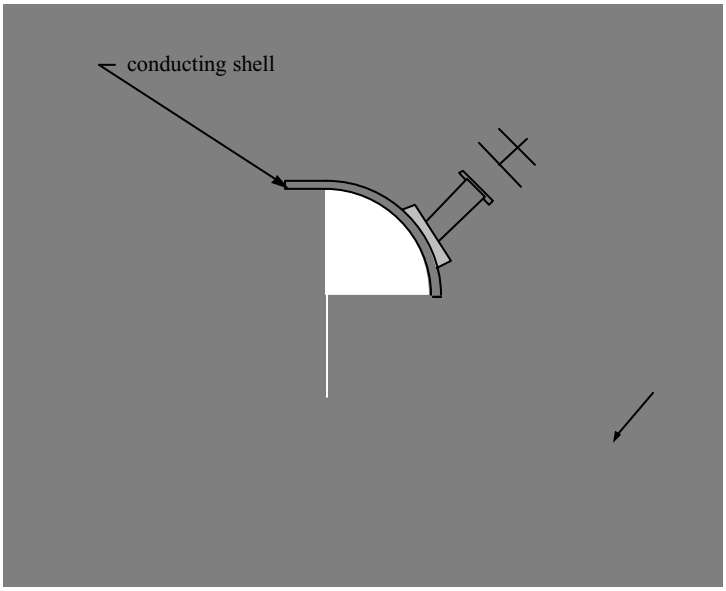

.

Fig 1.2 Vacuum chamber with conducting shells

Another unique feature of the HBT-EP tokamak is a set of coils powered by an 10 MW amplifier provided by the Los Alamos National Lab. The coils are wound in saddle shape and located at different toroidal positions to provide a magnetic filed with m/n = 2/1 structure. Shown in figure 1.3 is a schematic of the saddle coil and their locations on HBT-EP tokamak.

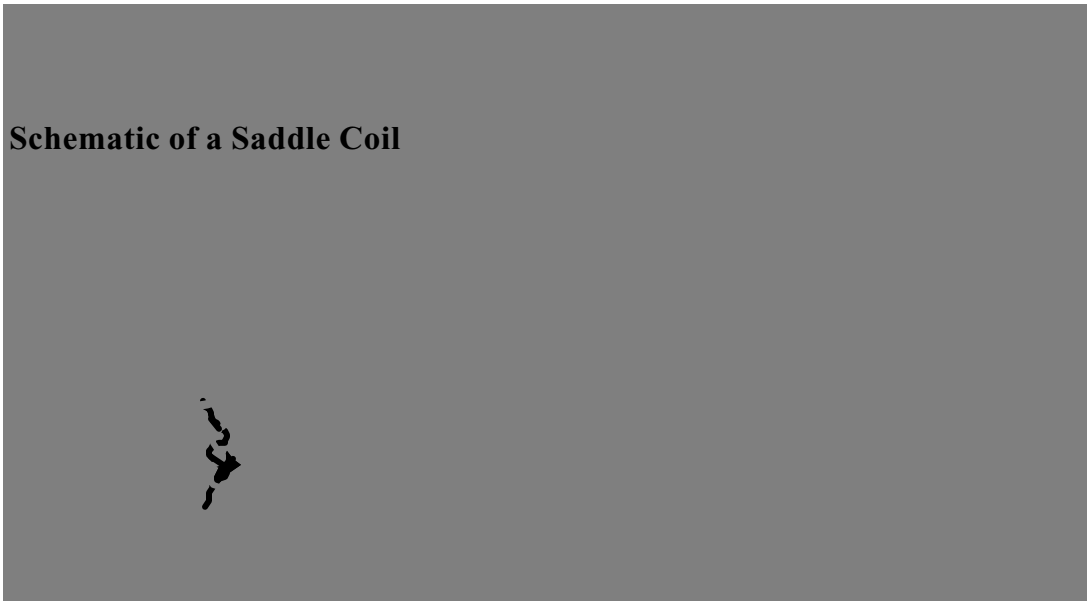

Fig. 1.3 Saddle coils

The physics goals of HBT-EP are:

1. Demonstrate passive stabilization of β-limiting, rapidly growing disruptive MHD instabilities using the movable, close-fitting conducting shells described above. Experimental results showed that discharges reach higher values of beta without disruption when the conducting walls are moved close to the surface of the plasma [4, 5, 6, 7, 8].
2. Demonstrate active control of residual slower growing modes using external saddle coils and power amplifiers. The magnetic fields from the saddle coils provide the means to investigate both asynchronous and synchronous feedback. Experiments show acceleration or deceleration of the frequency of slowly growing modes and mode amplitude reduction during brief intervals of phase synchronism [5].

This thesis presents the mode structure measurements of m = 2, n = 1 in the context of these experiments.

1.4 MHD mode structure measurement and soft X-ray tomography

The key diagnostic in this thesis is the 32 channel soft X-ray tomography system. A special segment of vacuum chamber with 32 viewing ports was built. One soft X-ray sensitive photodiode is mounted on each port, thus the photodiodes are distributed uniformly both in r and θ directions, providing 32 collimated viewing chords through the plasma cross-section(see figure 1.4). The photodiodes are coated with a specially designed thin film filter consisting of 100nm Zr, 7.5nm Ti and 75nm C to filter out the photons with energy lower than energy of soft X-ray[9]. Figure 1.4 shows the detector layout and the trasmission of the filter. Line-integrated soft X-ray emissivity from the 32 photodiodes can be feed into computer programs to give the 2-d profile of the soft X-ray radiation. Soft X-radiation is assumed to be approximately propotional to $n_e n_i T_e$, i.e., the product of ion density, electron density and electron temperature. Fluctuation of the soft X-ray radiation provides mode structure information of the MHD instabilities.

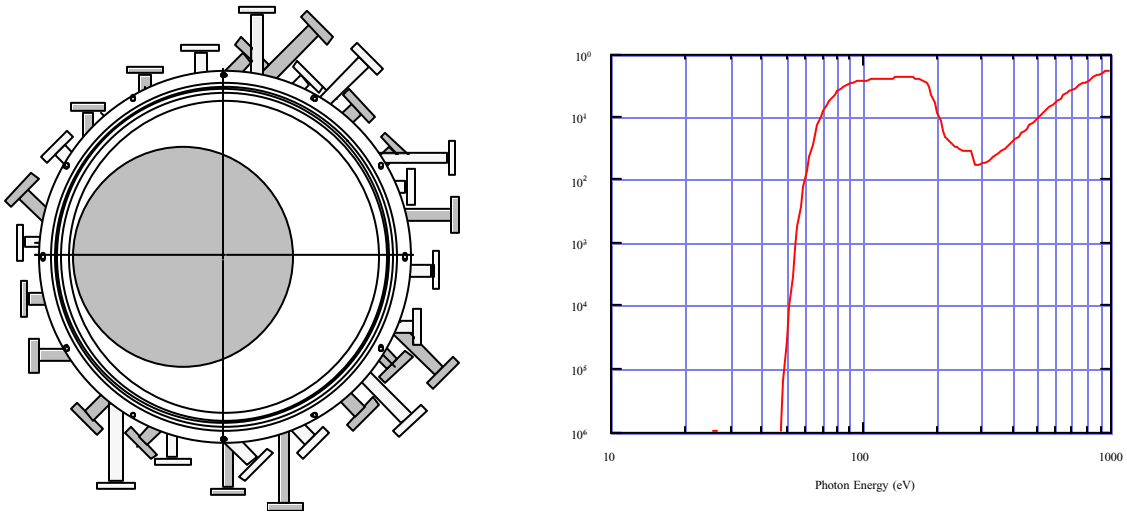

Fig. 1.4 the detector layout and the trasmission of the filter

1.5 Principle results

Experiments demonstrated that applied oscillating resonant magnetic fields with both single-phase and two-phase are capable of modulating the MHD mode rotation. When the frequency of the applied magnetic field changes, the mode rotation also changes. The dominant MHD modes were identified to have a m = 2 tearing structure. It is also observed that two-phase applied perturbations induced less instantaneous modulation of the mode rotation. A model taking into consideration the torque exchange between the applied perturbations and the rotating plasma at the resonant magnetic surface has been used to explain the rotation control by applied resonant magnetic field.

1.6 Outline of the thesis

Chapter 1 is a review of the theory of the applied resonant magnetic experiments. HBT-EP tokamak will be described in detail in chapter 3. Chapter 4 describes the

diagnostics available on HBT-EP. Soft X-ray tomography system will be discussed in more detail in chapter 5. Chapter 6 presents the more important data analysis methods for this thesis. Chapter 7 contains the analysis and principle results of this work. I will then summarize in chapter 8.

References:

[1] K. Miyamoto, Plasma Physics for Nuclear Fusion, (MIT press, Cambridge, 1980).

[2] A.D. Sakharov and I.E. Tamm, Plasma Physics and the Problem of Controlled Thermonuclear Reactors, (Pergamon, NY 1959-1960), Vol 1 first three articles.

[3] L.A. Artismovich, Nuc. Fusion **12**, 215 (1972).

[4] M.K.V. Sankar et al., J. Fusion Energy **12**, 303 (1993).

[5] T.H. Ivers et al., Plasma Physics and Controlled Nuclear Fusion Research **1994** IAEA, Seville (1994).

[6] D. Gates, Ph.D. thesis, Columbia University, 1993.

[7] R. Kombargi, Ph.D. thesis, Columbia University, 1997.

[8] A. Garofalo, Ph.D. thesis, Columbia University, 1997.

[9] Qingjun Xiao and G. Navratil, Rev. Sci. Inst. **67**, 3334 (1996).

Chapter 2

Theory of Applied Resonant Magnetic Perturbation Experiments

In this chapter, a numerical model for the applied resonant magnetic perturbation experiments is reviewed. The evolution of perturbed magnetic field is determined by the field component of the saddle coils. The dynamics of plasma rotation takes into account saddle coil force, wall drag and viscous force.

2.1 Introduction

In tokamaks, both high density and low-q operation are limited by disruptions, which involve a sudden loss of confinement and plasma current. A large amount of energy is dumped on plasma facing components and large electromechanical forces are induced. It is generally accepted that density limit, low-q and current rise disruptions are connected to the non-linear evolution of the resistive tearing modes with mode numbers m=2, n=1 [1, 2].

An important problem in nuclear fusion research is the design of an active control method capable of preventing the growth of these MHD instabilities through the control of rotation or active feedback[3]. Through controlled rotation, one can study the phenomenon of locked mode. A favored rotation velocity profile in a tokamak also has the potential of being insensitive to error fields due to imprecise coils, and of suppressing of certain forms of turbulence and toroidal Alfven eigenmodes[4].

In order to propose suitable designs for the control drivers it is necessary to have a dynamic model of the process to be controlled. One of such models includes all the relevant transient effects and is valid for any arbitrary time variation of the current supplied to the coils by the amplifiers [5]. This is the model that will be reviewed in this chapter. Starting from a classical model of tearing mode evolution the equations of the magnetic island amplitude growth and then rotation of the mode are cast in a suitable form using a space phasor model. A suitable schematisation can be obtained on the basis of the two axis theory of electrical machines, leading to simple and compact equations with a significant physical picture, and in a form useful for engineering purposes. Reference [4] contains a discussion of other models.

2.2 Mode growth

The effect of plasma finite resistivity η at rational surfaces allows the growth of helical magnetic lines of force which modify the topology of the nested axisymmetric confinement magnetic surfaces. Rotating magnetic islands appear and they are identified by the helical coordinate $m\chi_W = m\theta_W - n\phi_W$, where θ and ϕ are respectively the poloidal and toroidal coordinates. The evolution of a general helical magnetic perturbation, δB_r, is governed by Farady's Law and Ohm's law coupled with the quasineutrality condition $\nabla \bullet J = 0$, produces a torque driving fluid vortices near the q rational surface [6].

In the nonlinear phase the perturbation develops magnetic islands of width related to the equilibrium shear q'/q and poloidal field $B_{\theta 0}$:

$$W = 4\sqrt{\frac{qr_s}{mq'}\frac{\delta B_r(r_s)}{B_{\theta 0}}} \qquad (2.1)$$

The island growth is determined by integrating the diffusion equation for δB_r over the island width resulting in [7]:

$$\frac{dW}{dt} = \frac{\eta}{2\mu_0}\Delta'(W) \tag{2.2}$$

where:

$$\Delta'(W) = \frac{\partial \ln(\delta B_r)}{\partial r}\Big|_{r=r_s} \tag{2.3}$$

in which r_s is the radius of the rational surface.

In the presence of external multipolar fields (and passive conductors) B_c, the plasma frozen into islands is subject to a torque which determines the evolution of the phase $\phi_w(t)$, according to momentum balance in the toroidal direction:

$$m_i R_0 \frac{d^2\phi_w}{dt^2} = R_0\mu_0^{-1}\int \underline{e}_\phi.(\nabla\times\delta\underline{B})\times(\delta\underline{B}+\underline{B}_c)dv \tag{2.4}$$

in which R_0 is the major radius and m_i is the ion mass which is an approximation of the plasma mass.

2.3 Rotation model

To control the growth of the most dangerous modes, with helical mode numbers m=2, n=1, it is necessary to apply an externally controlling field rotating with the same frequency of the mode and locked in phase with it [8]. The mode used in the design of a control system can be approximated because changes in parameters are damped by the control scheme. However the control model must embody all the dynamic effects occurring during the evolution of the transient phase. It should also be valid for any

arbitrary time variation of the current generated by the amplifiers feeding the coils. The main assumptions used in the model are:

1. The magnetic islands appearing at the q = m/n surface are frozen in the plasma and rotate with it.
2. Island rotation is modeled assuming a rigid rotor configuration with perturbation currents lumped in the islands.
3. Four conductors, $\pi/2$ radiance apart, inside the resistive vessel simulate the effects of the controlling saddle coils.
4. Island rotation is damped by eddy currents effects in the wall and a phenomenological viscosity between the islands and the rest of the plasma.

A suitable schematisation can be obtained by means of the two-axis theory of electrical rotating machines, which gives simple and compact equations with a significant physical picture. The helical coordinate χ is replaced by the electrical angle $\alpha=m\chi$, with 2π periodicity, and mapped on a circle (Figure 2.1), The axis defined by the O-points of the magnetic islands (where the plasma perturbation currents are modeled using lumped parameters) in the α-r plane is called plasma quadrature axis q. The axis orthogonal to it is called the plasma direct axis d.

In the mode rotating reference frame the mode amplitude and rotation rate equations are:

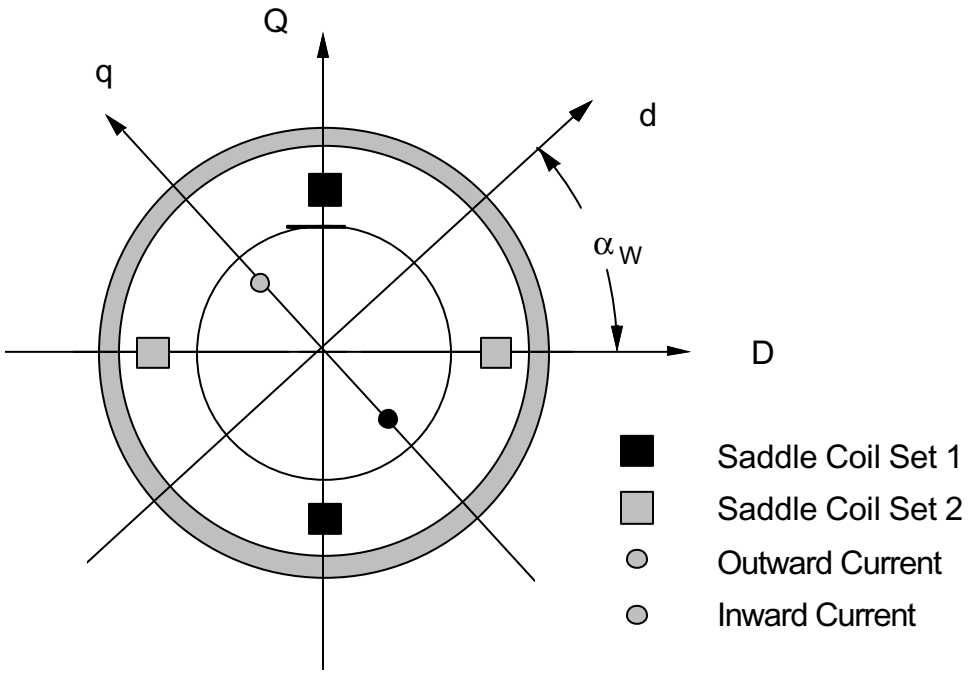

Fig. 2.1 Space phaser vector model

$$\frac{d(\delta B_{r)}}{dt} = K_{BS}\left[1-\sqrt{\frac{\delta B_r}{B_{SAT}}}\right]\sqrt{\delta B_r} + K_{BC}\frac{B_{Cd}}{\sqrt{\delta B_r}} \tag{2.5}$$

$$\frac{d\omega}{dt} = K_{TC}\delta B_r B_{Cq} - K_{TE}\delta B_r^2 \frac{\omega\tau_v}{m^2+\omega^2\tau_v^2} - K_{TV}(\omega-\omega_0) \tag{2.6}$$

where:

$$K_{BS} = \frac{\eta}{2m\mu_0}\Delta'(0)\sqrt{\frac{mq'B_{\theta 0}}{qr_s}}, \tag{2.7}$$

$$K_{BC} = \frac{2m}{r_s\Delta'(0)}K_{BS} \tag{2.8}$$

and

$$K_{TC} = \frac{8\pi mR_0}{\rho V\mu_0}, \tag{2.9}$$

$$K_{TE} = 16\frac{\pi r_s^2 R_0}{\mu_0}\left(\frac{r_s}{r_v}\right). \qquad (2.10)$$

B_{SAT} is the saturated level of the δB_r. The saddle control field components B_{cd} and B_{cq} in the rotating reference frame are responsible respectively for the control of the mode growth and phase; ρ is the plasma mass density and B_{SAT} is the natural saturation level of the mode, corresponding to $\Delta'(W_{SAT})=0$ and depending on the equilibrium current profile and plasma parameters. The constant τ_v is the vessel penetration time, r_v is the vessel minor radius, and ω_0 is the plasma rotation speed. Note that rotation speed is strongly dependent on the method of plasma heating.

Let

$$b = \frac{\delta B_r}{B_{SAT}},$$

$$b_d = \frac{\delta B_{Cd}}{B_{SAT}},$$

$$g_1 = \frac{K_{BS}}{B_{SAT}},$$

$$g_2 = K_{BC}\sqrt{B_{SAT}},$$

$$h_1 = \frac{K_{rc}B_{SAT}^2}{\omega_0},$$

$$h_2 = K_{TE}B_{SAT}^2,$$

and

$$h_3 = K_{TV}.$$

Then

$$\frac{db}{dt} = g_1(1-\sqrt{b})\sqrt{b} + g_2\frac{b_d}{\sqrt{b}}, \tag{2.7}$$

and

$$\frac{d\varpi}{dt} = h_1 b b_q - h_2 b^2\left(\frac{\varpi\tau_w}{m^2+\varpi^2\tau^2}\right) - h_3(\varpi-1). \tag{2.8}$$

By sovling equations (2.7) and (2.8), we can find oscillating field, phase and frequency as functions of time.

References:

[1] J. C. Hosea, et. al., in Plasma Physics and Controlled Nuclear Fusion Research, Madison, 1970 (International Atomic Energy Agency, Vienna, 1971), Vol. II, p.425

[2] J. A. Wesson, et. al., Nuclear Fusion, 29, 641 (1989)

[3] E. Lazzaro, et. al., Physics of Fluids 31, 1623 (1988)

[4] T. H. Jensen, et. al., Phys. Fluids B, 5, 1239 (1993)

[5] G. D'Antona, IEEE Transaction on Nuclear Science, Vol. 41, No. 1, February 1994

[6] H. P. Furth, et. al., Physics of Fluids 16, 1054 (1973)

[7] P. H. Rutherford, Physics of Fluids 16, 1903 (1973)

[8] J. K. Lee, Nuclear Fusion 23, 63 (1983)

Chapter 3

THE HBT-EP Tokamak

The High beta Tokamak-Extended Pulse (HBT-EP) experiment was designed to investigate the feasibility of a stable, high-ß tokamak using the combination of plasma rotation, a close-fitting conducting wall and active mode control[1, 2, 3, 4, 5]. This chapter describes the hardware components of the HBT-EP experiment. Please also refer to [3, 4, 5] for more of the descriptions of HBT-EP hardware.

3.1 Overview

HBT-EP tokamak was built to study MHD instabilities during high β discharges. It has a major radius of 92 cm, and a minor radius of 14 - 19.3 cm. The plasma current is usually less than 25 kA. The machine runs with a pulse length less than 10 ms. The toroidal field is about 3 kG. The line integrated plasma temperature is about 100 eV. The plasma density is 1 x 10^{13} cm^{-3}. The vacuum chamber was constructed from ten large stainless steel sections linked at five locations by stainless steel bellows and "spool" segments housing the poloidal limiters and diagnostic ports. The remaining chamber segments are linked by quartz cylinders which permit rapid penetration of the Ohmic heating flux and equilibrium fields. In addition, the quartz segments serve as locations for Fourier analyzing Rogowski coils, Mirnov loops, and high power saddle coils.

One of the unique features of HBT-EP is a segmented conducting shell which consists of 20 segments located at 10 toroidal locations. Each segment is attached to a

shell positioner, so the distance between the shell and the plasma can be adjusted between shots. This unique feature allows us to study the wall stabilization effect on MHD instabilities. Another unique feature of the HBT-EP tokamak is a set of saddle coils powered by an amplifier provided by Los Alamos National Laboratory. The saddle coils are located at different toroidal positions to provide a magnetic filed with m/n = 2/1 structure. They allow us to carry out controlled feedback studies on the MHD modes.

3.2 Magnetic Field Coils

HBT-EP utilizes the toroidal field coils from the CLEO tokamak/stellerator of Culham laboratories [6]. A fast ohmic heating system enables a rapid discharge startup. A flexible poloidal field coil system permits control of plasma position and shape.

3.2.1 Toroidal field (TF) system

The toroidal field (TF) coils are a set of twenty 64 turn copper coils (each coil consists of two 32 turn coils, side by side) located inside stainless steel dewers which in turn are surrounded by large aluminum casings. The total inductance of the coil set is 0.235H with a resistance of 0.635? . A 10kV, 0.04 Farad (2MJ) capacitor bank powers these magnets. The peak field that is attainable with the current TF system is 0.5 Tesla. Figure 3.1 is a top view showing the TF coils, transformer coils, vacuum vessel and the locations of various diagnostics. The twenty TF coils are grouped into ten coil pairs each linked by one of the ten large vacuum chamber segments (described later in the chapter). This modular arrangement allows each chamber/magnet pair to be handled separately, facilitating maintenance and disassembly. The centering forces on the TF coils due to

higher field on the inside of the torus are opposed by a central cylinder made of aluminum and G-10 fiber glass epoxy. The moments arising from the interaction of the vertical field and the TF currents are taken up by large stainless steel turnbuckles between the coils. A silican based dielectric fluid is circulated in the cavity originally used for liquid nitrogen for coolant. The coil heat increase of $5^{\circ}C$ at full energy (2MJ) is removed by chilling the fluid with a 23,000 Btu/hour chiller.

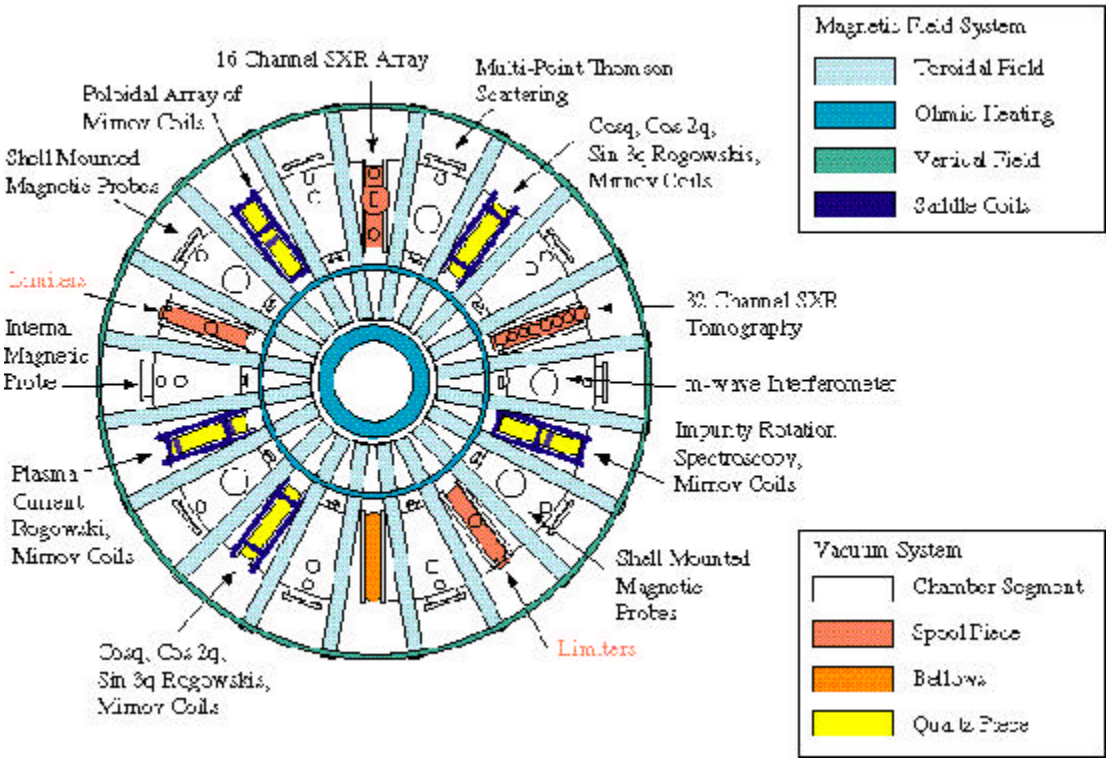

Fig 3.1 Top view of HBT-EP showing magnet configuration, vacuum chamber components and diagnostic location

3.2.2 Poloidal field (PF) system

The poloidal field setup on HBT-EP [3] includes both the ohmic heating (OH) and the vertical field (VF) systems, see Fig 3.2. The OH transformer consists of a six turn air core coil set. The central four turns (OH1) are one unit, cast in an epoxy ceramic composite. The upper and lower turns (OH2) are free standing copper coils mounted on the TF magnets. All the turns are fabricated from OFHC grade copper with a cross section of 0.5" by 3.5". The coil inductance is $15\mu H$.

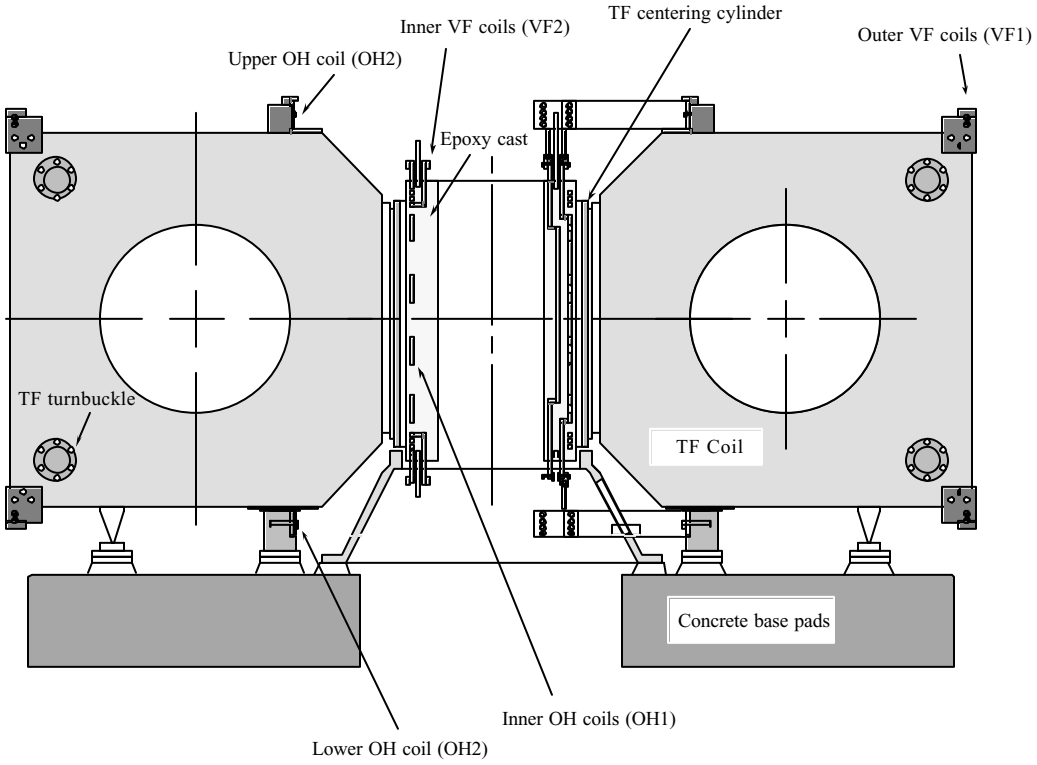

Fig 3.2 Cross sectional view of the HBT-EP principal coils

The VF coils consist of two outer (VF1) two turn coils supported on the TF magnets and two inner (VF2) three turn compensation coils located in the epoxy cast of the OH coil. The outer coils are made of double strands welding cable and have a radius

of 157 cm, with a vertical separation of 129 cm between them. The inner coils are made of OFHC grade copper with a cross section of 0.5" by 0.5", they have a radius of 27 cm, with a vertical separation of 80 cm between them.

The VF2 sections potted in the OH1 coil are wound anti-parallel to the VF1 parts. The current in the inner coils flows in the opposite direction to the current in the outer coils. The purpose of these inner VF2 segments is to eliminate the mutual inductance between the VF and OH coils by making flux that opposes the coupled flux from the outer VF coils. The air core ohmic heating coil is built to minimize the poloidal field within the plasma and allows fast current start up with rise times of $\approx 100\,\mu s$.

The OH and VF coils are powered, similarly to the TF coils, by capacitor banks. Some details on their designs and construction can be found in reference [3]. In order to initiate a typical plasma discharge, the air core OH transformer is charged with a negative bias current (bias bank) with a rise time of $\approx 500\mu s$ followed by a fast start current (start bank) with a rise time of $\approx 150\,\mu s$, permitting the formation of the plasma discharge faster than the magnetic diffusion time. A one Farad electrolytic power crowbar sustains the loop voltage. A low power electron gun provides free electrons to aid in plasma breakdown. See section 3.5 for detail description of the electron gun. The VF bank (fast start bank followed by a power crowbar) is fired at the same time as the OH start bank.

3.3 Vacuum system

The HBT-EP vacuum chamber maintains an ultra high vacuum consistent with low impurity fraction, especially oxygen control so as to achieve high temperature operation at the Troyon β-limit. The vacuum vessel also supports an adjustable

conducting wall used for equilibrium and external kink stability. The chamber incorporates rapid soak-through of the poloidal fields, reduction of the peak electric field during the breakdown of the plasma, good diagnostics access, and easy assembly.

3.3.1 Vacuum vessel segments

The complete vacuum vessel is shown above in the top view schematic of HBT-EP, Fig 3.1. The vacuum chamber consists of ten large wedge shaped stainless steel segments, see Fig 3.3. These are made from standard 20" diameter 90° pipe elbows. Each of these ten segments is terminated by large stainless steel end flanges on either side. These are at an angle of 36° relative to each other. All the ports on the vessel use copper sealing gaskets so as to eliminate the permeation of air that occurs with O-ring seals.

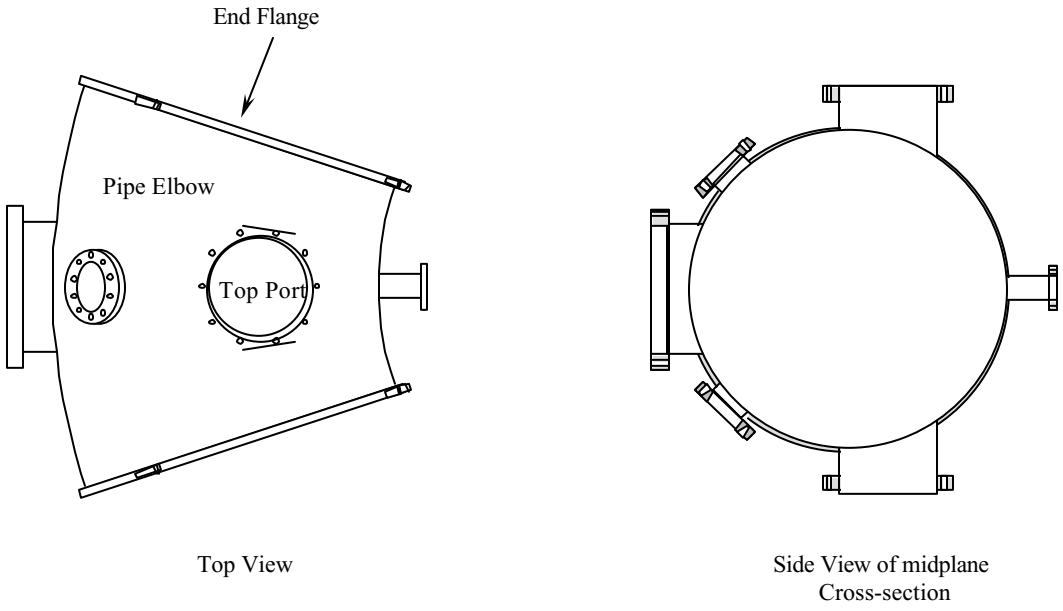

Fig 3.3 HBT-EP vacuum vessel segment

The ten chamber sections are joined by three different kinds of transition segments: insulating portions made of straight quartz tubing (18" diameter, 11 cm long),

stainless steel spool pieces and stainless steel flexible bellows sections. Quartz sections are compatible with ultra high vacuum requirements. They are transparent and thus provide access for visible radiation diagnostic measurements. They also are a preferred location of magnetic fluctuation diagnostics because fields rapidly penetrate non conductors. The spool pieces have ports in them for diagnostics and limiter support. The bellows segments' flexibility absorbs manufacturing errors in the circumference of the vessel. All the transition pieces attach to the vacuum vessel with a double pumped O-ring seal. The region between the two O-rings is pumped on by a mechanical pump to reduce permeation through the inner O-ring.

The ten vacuum chamber segments are each supported both horizontally and vertically. From the inside of the vacuum vessel to the TF centering ring, a radial support beam opposes the vacuum centering force. From the cement base pad to the lower end of a vacuum chamber section, two vertical support beams (one on each side) oppose gravity. These supports are electrically insulated with G-10 fiber glass, they prevent relative motion between the segments themselves and between the segments and the support structure.

3.3.2 Pumps and controls

The HBT-EP vacuum chamber is evacuated with two cryo pumps with effective speeds of $\approx 2000(l/s)$, one turbo-molecular pump with a lower effective speed of $\approx 1000(l/s)$ and a series of back up mechanical pumps behind the turbo pump. Initial pump down procedures are started with a mechanical pump followed by the turbo pump bringing the machine to pressures of $\approx 10^{-5} Torr$ before switching to the cryo pumps

which lower the pressure to the ultra high vacuum levels ($\approx 10^{-8} Torr$) of HBT-EP's operation. The entire system of pumps, valves, gauges and other monitors (e.g. vacuum measurements, power measurements, air pressure etc.) is centrally controlled by a vacuum system control panel.

3.3.3 Vacuum conditioning

After the pumping down of the vacuum chamber, the inside walls of the vessel must be conditioned, essentially water and oxygen have to be removed from the vacuum surfaces. The goal is to reach base pressures of $\approx 10^{-8} Torr$ with oxygen partial pressures of $\leq 10^{-12} Torr$. The two cleaning procedures used are chamber baking and glow discharge cleaning.

The baking of each vacuum chamber segment is done using two (top and bottom) of the forty separate insulating heating pads. The temperature of the vessel rises to a maximum of $110^{\circ} C$. It is regulated with ten separate controllers (one for each segment) and the total power available for the heating system is 20kW.

Glow discharge cleaning[4] involves filling the vacuum vessel with either deuterium or helium, in the tens of milliTorr range, and initiating a discharge in the chamber using an electrode that is inserted into the center of the vessel. The electrode is DC biased positive with respect to the walls of the chamber. The vessel is filled with a neutral gas, such as deuterium, and when the breakdown occurs, an electrical circuit consisting of the electrode, the ionized gas and the chamber walls forms. The current in this closed circuit is an ion current and it is drawn to the walls. The ions then react with the adsorbed impurities in the walls and the impurities are knocked off the wall by

striking ions. The power supply typically gives out 0.7A at 600V through a current limiting resistor of 250? with a Deuterium fill pressure of $10 mTorr$.

3.4 Limiters

The size of the plasma in HBT-EP is determined by the location of the top, bottom and outside adjustable stainless steel rail limiters. These are located at two toroidal locations, see Fig 3.5. The inner edge of the plasma cannot be smaller than 75 cm since the stainless steel flanges on the vacuum vessel segments act as inner limiters.

The limiters are made from 3/8" thick type 316 stainless steel plates. The radial adjustable limiter has a range of motion of 10.8 cm which allows outer plasma radii from 103.1 cm to 113.9 cm. The vertical adjustable limiters have a range of motion of 4.6 cm which allows minor radii between 14.6 cm and 19.2 cm. In addition to the movable limiters at each location, there are fixed limiter blades to prevent current from flowing through unconfined plasma behind the limiters during small major-radius operation. The movable limiter positioner assembly consists of stainless steel rods that attach to the blades on one end and to sealing Con-Flat flanges on the other end. Between the end Con-Flat flange and the machine port, a stainless steel welded bellows supported by four threaded rods with jack screws accurately place the limiter blade at the desired radial position. The range of plasma aspect ratios achievable is A=4.9-6.3.

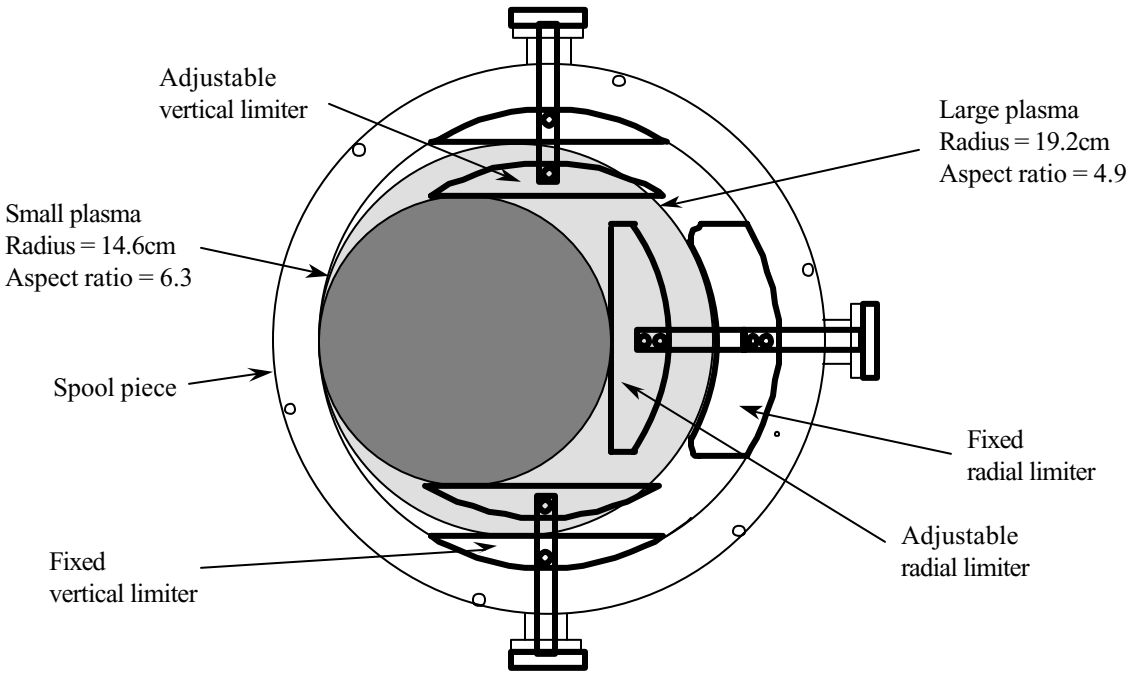

Fig 3.5 Cross sectional view of HBT-EP's adjustable limiters

3.5 Electron Gun

An electron gun has been built to provide free electrons before the plasma discharge to aid in plasma breakdown. Magnetron scheme has been chosen for the design to take advantage of the magnetic and electric fields in tokamak. The basic principle of the magnetron gun is the following: Electrons pulled out from the cathode gyrate around the magnetic field. Since there is also a component of the electric field in the direction of the magnetic field, the electrons are extracted away from the tip of the electron gun. A detailed review of magnetron design can be found in [7].

The cathode of the electron gun is a coiled filament made of 7 cm long and 0.15 cm thick tungsten wire. It is heated by 60 Hz AC power through an isolation transformer and a 6:1 step-down transformer, hence the voltage applied to the tungsten wire is

approximately 20V AC. A pulse circuit triggered by an SCR is applied across the cathode and the anode. It provides a voltage pulse of 400V in amplitude and a pulse length about 200μS. Fig 3.6 is a schematic of the whole circuit.

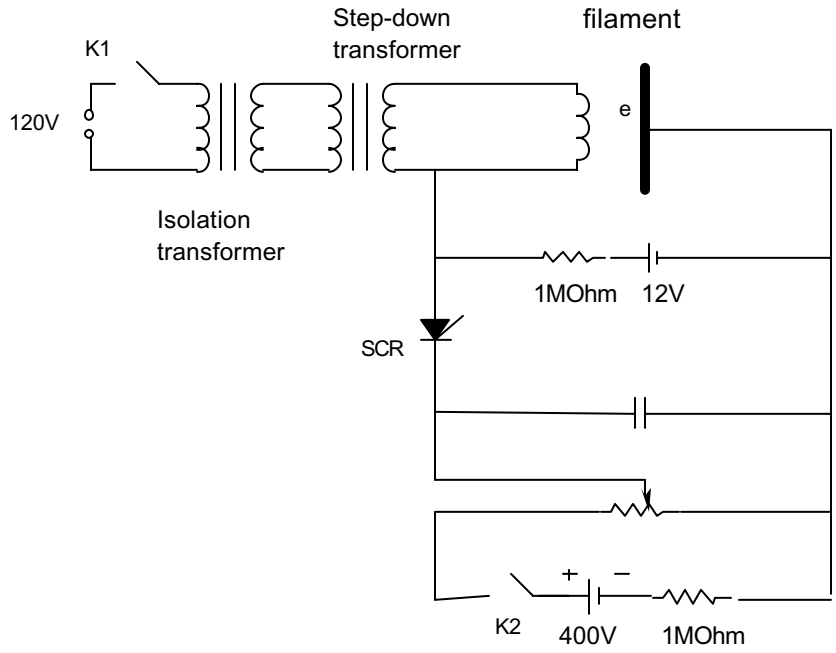

Fig 3.6 Electron gun circuit

The electron gun is mounted on a 10 inch port on the top of the machine. A stainless steel bellows in conjunction with a gate valve and a leak valve allows moving the tip of the gun to different positions and the taking off for repair without disturbing the vacuum. Fig 3.7 is an assemble drawing of the electron gun.

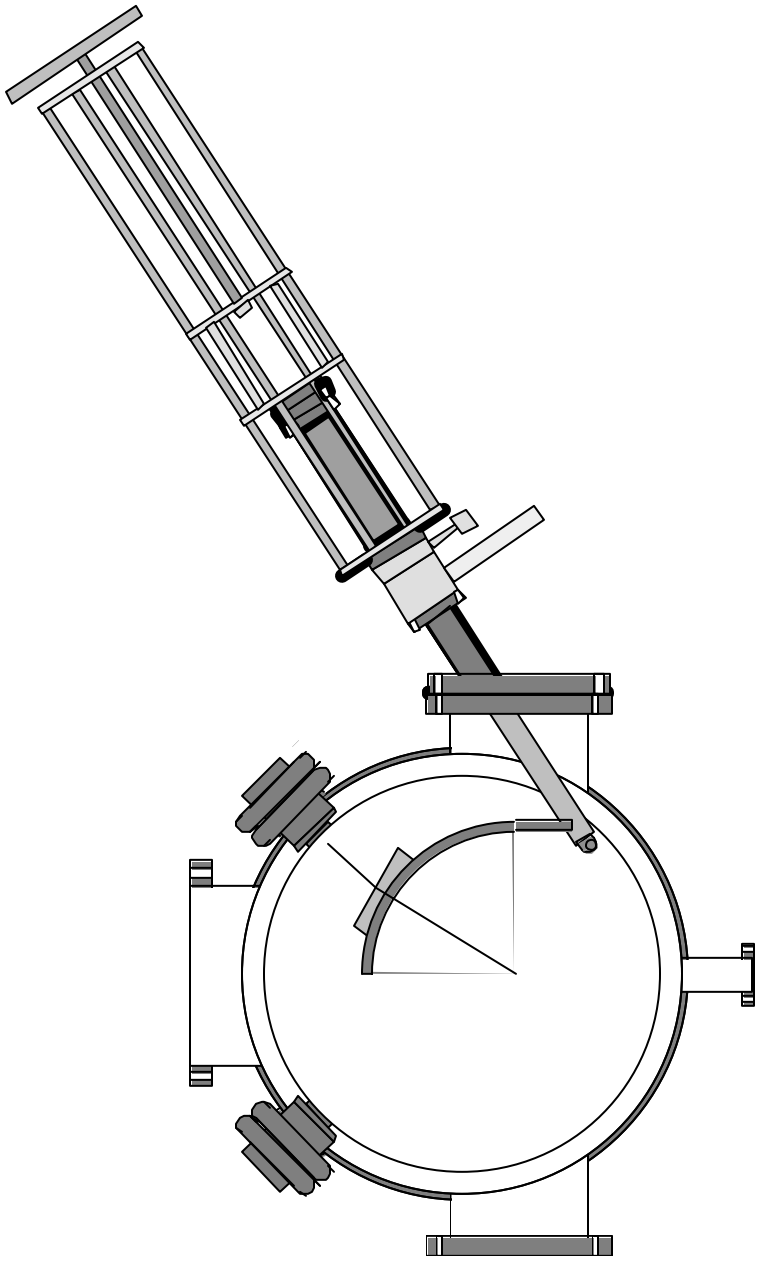

Fig 3.7 Electron gun

3.6 Conducting walls

The HBT-EP approach to the study of passive and active control of MHD instabilities begins with internally mounted and electrically isolated modular adjustable conducting walls. These segments or *shells* are made of 0.013m thick spun aluminum with a 0.002" thick coating of pure unpolished Nickel, which is selected as a plasma facing material due to its low sputtering yield. The major radius of the wall is $R_0 = 92cm$,

and its minor radius is $b = 16cm$, which puts it 1 cm away from HBT-EP's small-type plasma configurations $(R_0 = 92cm,\ a = 15cm)$. The wall consists of 20 separate sections, two in each of the ten large vacuum chamber portions. They are individually mounted at the end of a movable positioner. The conducting plates are located, at a $\pm 45^{\circ}$ angle to the mid-plane of the torus, see Figure 3.8.

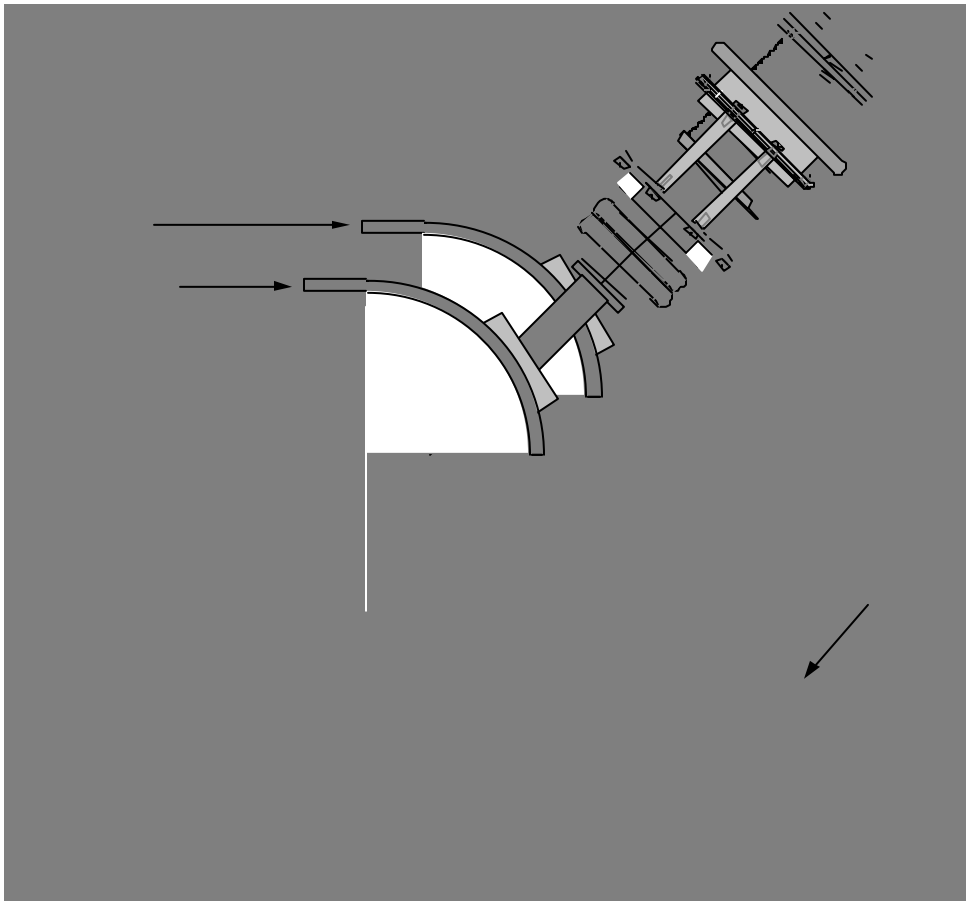

Fig 3.8 Vacuum vessel with conducting wall

When the limiters are fully inserted, the plasma minor radius a is fixed and the conducting wall position can be varied over a range of 0.01-0.09m from the surface of the plasma ($1.07 \le b/a \le 1.52$, where b is the radial distance of the conducting plates from

the plasma center), see Fig 3.9. The conducting wall segments are shaped specifically for circular cross sectional plasmas, they cover up to 78% of the plasma surface when all 20 of them are fully inserted.

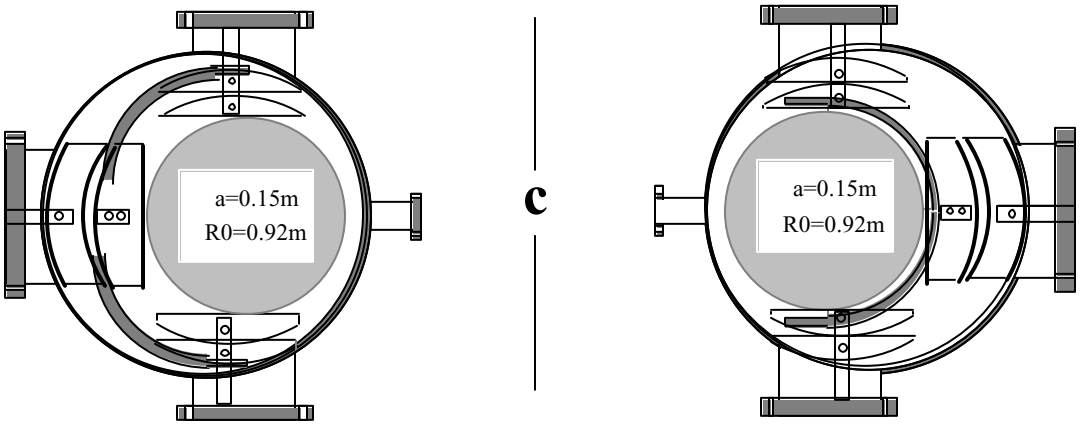

Shells retracted: <b>/a = 1.52

Shells inserted: b/a = 1.07

Fig 3.9 HBT-EP's vacuum chamber cross section showing poloidal limiters and conducting shells in the inserted and retracted configurations

3.7 Saddle Coils

Active control of MHD instabilities and induced plasma rotation are accomplished through the application of resonant magnetic perturbations imposed by a set of modular saddle coils. The coil array consists of five, nine-turn coil pairs. Each pair spans 6^{O} in toroidal angle and generates a magnetic perturbation of dominant poloidal mode number m = 2. The coils are connected in series and mounted outside each of the five quartz vacuum chamber segments, which gives the applied field a toroidal mode number of n = 1. Fig 3.10 is a top view of the HBT-EP tokamak showing the locations of the saddle coils. It also shows a schematic of one saddle coil pair. The coil set is driven by two 10 MW power amplifiers[8] provided under a collaboration with Los Alamos National Laboratory. The amplifiers are transformer coupled to the saddle coils, and are

capable of delivering ±600 A current with a bandwidth of 20 kHz. Fig 3.10 shows a frequency scan and the spectrum of the saddle coils. The frequency scan shows good radial field penetration through quartz gaps. The saddle coil spectrum shows, that the m = 2, n = 1 resonant component is four times larger than next resonant term.

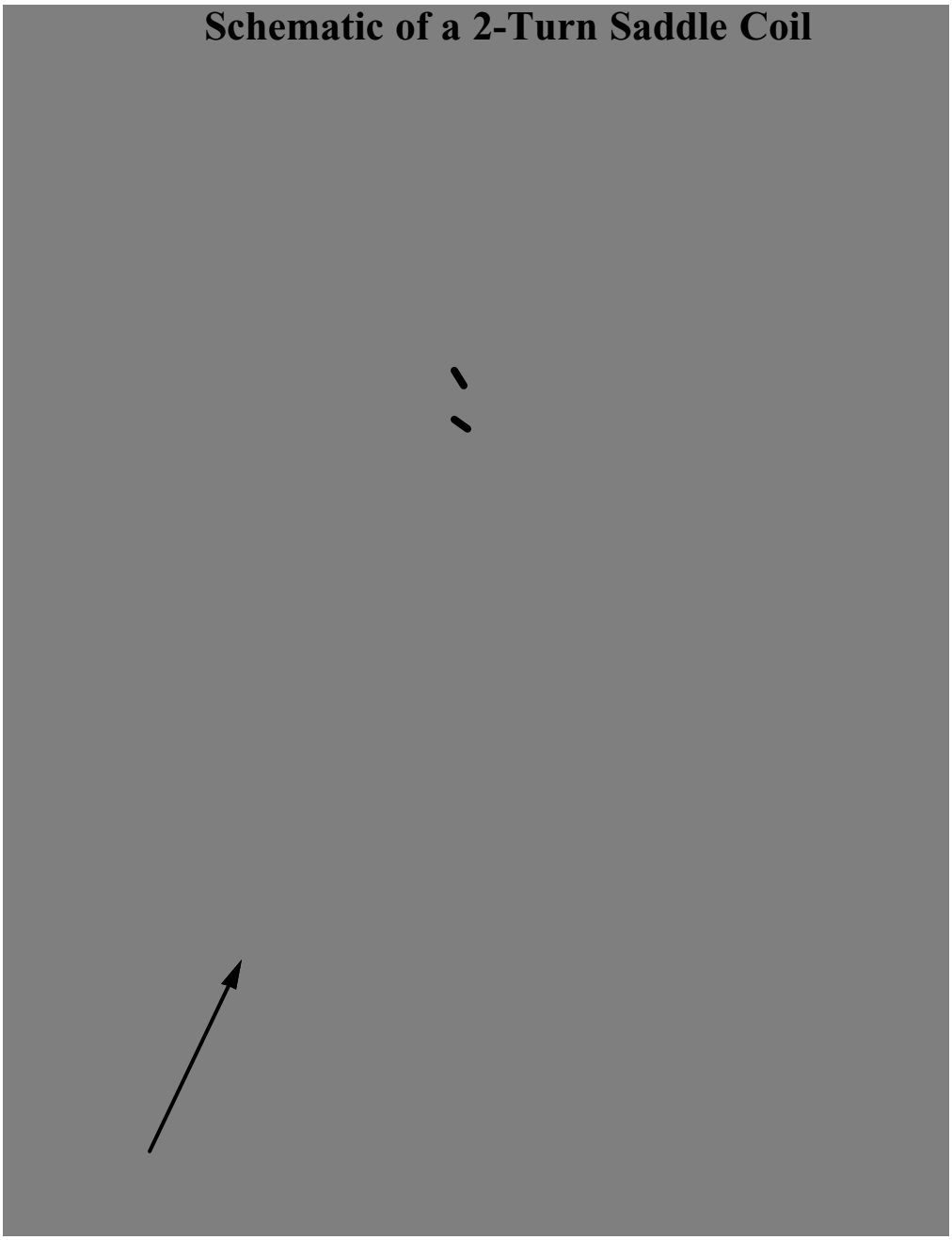

Fig. 3.10 Saddle coil location and Schematic

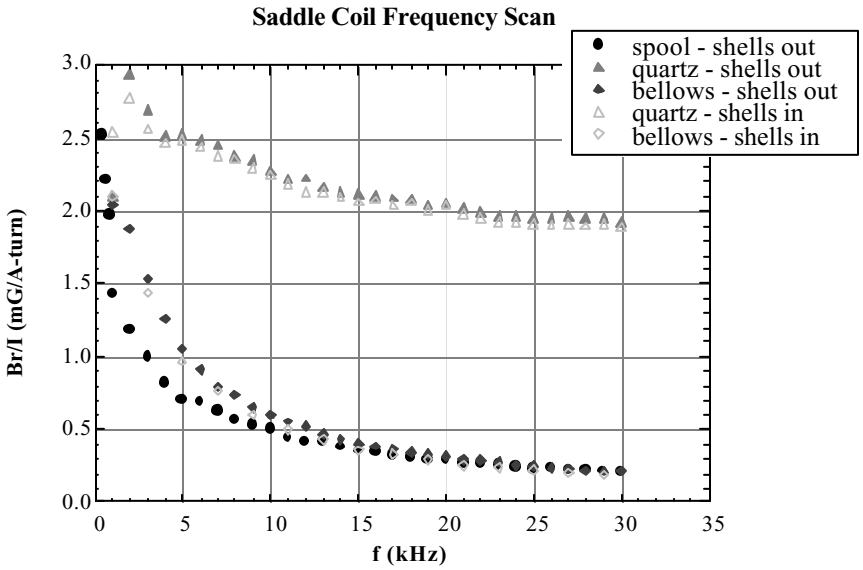

Fig. 3.11 Saddle spectrum

References:

[1] M.K.V. Sankar et al., J. Fusion Energy **12** 303 (1993).

[2] T.H. Ivers et al., Plasma Physics and Controlled Nuclear Fusion Research **1994** IAEA, Seville (1994).

[3] D. Gates, Ph.D. thesis, Columbia University, 1993.

[4] R. Kombargi, Ph.D. thesis, Columbia University, 1997.

[5] A. Garofalo, Ph.D. thesis, Columbia University, 1997.

[6] D.R. Robinson et al., Plasma Physics and Controlled Nuclear Fusion Research **1986** IAEA, Kyoto (1986).

[7] R. Chatterjee, Elements of Microwave Engineering, Halsted Press, 1986.

[8] W. A. Reass, et al., in Proceedings of the 12th Symposium on Fusion Engineering, Monterey(Institude of Electronics and Electrical Engineers, New York, 1987)

Chapter 4

Diagnostics on HBT-EP

HBT-EP tokamak is well equipped with various diagnostics. To measure the plasma current, plasma position, loop voltage, magnetic fluctuations, total radiated power, soft X-ray flux, we have built several types of magnetic diagnostics, a 16 channel soft X-ray array and a soft X-ray tomography system. We are also working on a Thompson scattering system to measure plasma temperature profile, Mach probes and a spectroscopy diagnostic to measure plasma rotation. In this chapter, I will describe the magnetic diagnostics, the broadband radiometer and the 16 channel soft X-ray array. Soft X-ray tomography will be described in Chapter 5. A layout of all the available diagnostics is displayed in Fig. 3.1.

4.1 Magnetic diagnostics

Magnetic diagnostics are essential in understanding the MHD equilibrium and stability properties of tokamak plasmas. HBT-EP uses 136 magnetic probes. Some are inside the vacuum and some outside. Some are used for local measurements and others are used for global plasma measurements.

4.1.1 Internal magnetic probes

The magnetic field inside the plasma are measured using 13 vertical field coils and 2 radial field coils supported on a G-10 form encased in a thin stainless steel jacket. This multi-point magnetic probe is movable. It can be used to measure the field outside the plasma or it can be fully inserted into the core of the plasma to calibrate other diagnostics. This is done only when required since introducing the probe into the plasma deteriorates the performance of the discharge.

4.1.2 Global magnetic diagnostics

The most basic measurements are that of plasma current and position. These are made using Rogowski coils located around quartz sections of the vacuum chamber.

Total plasma current, I_P, is measured using a compensated Rogowski coil. This is a multiple turn solenoid that completely encloses the current to be measured. The transient plasma current generates a poloidal magnetic field which induces the detected voltage V. For a uniformly wound solenoid with N turns per unit length and a diameter d, V is given by the expression

$$V = N\pi\frac{d^2}{4}\mu_0\frac{dI_P}{dt} \tag{4.1}$$

A passive RC circuit integrates this voltage, from which the total plasma current, I_P, is deduced. A complete poloidal loop around the plasma would be sensitive to changes in the toroidal magnetic field, therefore one end of the solenoid is connected back through its center thus providing compensation for unwanted fluxes [1].

The same device can be used to measure plasma position by modifying the winding pitch of the basic solenoid. The Rogowski coil is wound with a density of turns proportional to the sine or cosine of the poloidal angle θ around the coil. Horizontal bulk

plasma motion is then detected by the $\cos\theta$ coil and vertical motion is given by the $\sin\theta$ coil. The signal from these coils is a function of the offset of the center of the current centroid from the geometric center of the sine or cosine coil [2]. For example, the expression for the cosine coil is given by

$$V_{coil} = f\left(R_{plasma} - R_{coil}\right)I_{\mathrm{P}} + K_{VF}I_{VF} + K_{OH}I_{OH} + corrections \tag{4.2}$$

The function f is taken to be a polynomial of order three. The K's are measured from vacuum shots. The corrections come from image currents that flow in conductors near the plasma, such as the vacuum chamber and the conducting wall segments. The coils are calibrated on the tokamak using the plasma position measured by the internal magnetic probe as a reference.

Rogowski coils with winding densities varying like $\cos(m\theta)$ or $\sin(m\theta)$ where $m > 1$ (e.g. m=2 or m=3) are used to observe MHD mode structures and their fluctuations prior to disruptions. The fluctuations we seek to measure are characterized by poloidal magnetic field perturbations having a mode structure defined by [3]

$$\tilde{B}_\theta = \mathrm{A}_{nm}\exp\left[i\omega_{nm}t - m\theta - n\Phi\right] \tag{4.3}$$

where $\tilde{B}_\theta$ is the oscillating component of B_θ, θ and Φ are the poloidal and toroidal angles, m and n are integers referred to as mode numbers and ω_{nm} is the angular frequency of the (m,n) mode in the frame of reference of the plasma. Therefore, the Rogowski coils measures the external azimuthal variation of the poloidal magnetic field B_θ, related to current-dependent plasma surface disturbances. B_θ, can be expressed as a sum of poloidal Fourier harmonics and a perturbation expansion can be done in the lab frame. The first order perturbed field, $\tilde{B}_\theta$, can be considered proportional to $\cos\theta$ or

$\sin\theta$ and the mth order term to the mth order Fourier harmonic and so on. The $\cos(m\theta)$ and $\sin(m\theta)$ coils instantaneously perform the Fourier analysis of the signals. The output from such coils (e.g. $\cos 2\theta$ or $\sin 3\theta$ of HBT-EP) is directly proportional to the time derivative of the required Fourier component. Only the m number of the mode is determined this way. For the n number, a phase comparison is done on two toroidally separated coils.

The plasma current produces a toroidal loop voltage as per Ohm's law. This single turn voltage is measured using flux loops (single-turn pick-up coils) that expand toroidally near the inner and outer radii of the vacuum vessel.

Figure 4.1 below illustrates typical measurements obtained on HBT-EP from the above described coils. In particular, the total plasma current, the plasma position, the loop voltage and signals from two Fourier-analyzing Rogowski coils sensitive to m=2 and m=3 magnetic fluctuations are shown respectively in parts (a), (b), (c), (d) and (e) of the plot.

4.1.3 Shell mounted probes

Shell mounted probes are small magnetic pick-up coils attached to the conducting wall. 72 coils are distributed at the central poloidal region on both sides of four HBT-EP conducting wall segments. Eddy-current measurements are made by calculating the difference between the magnetic fields located on opposite sides of a conducting wall section. By assuming that the thickness of the conducting plate is small compared with the scale lengths of the variation of the eddy currents, $\vec{\kappa}$, Ampere's law can be written as

$$\mu_0 \tilde{\vec{\kappa}} = \hat{n} \times \left[\tilde{\vec{B}}_{out} - \tilde{\vec{B}}_{in} \right] \tag{4.4}$$

where $\vec{\tilde{\kappa}}$ is the fluctuating surface current, $\hat{n}$ is the unit vector normal to the surface of the shells and ($\vec{\tilde{B}}_{out}, \vec{\tilde{B}}_{in}$) refer to the magnetic fields on the outer and plasma-facing side of the conducting wall. A more elaborate description of these coils is in [4].

4.1.4 External point probes

These are small external pick-up windings consisting of a poloidal array of 15 (B_θ, B_r) coils and a toroidal array of 5 (B_θ, B_r) coils. All are mounted on plastic supports just outside the five quartz vacuum chamber segments. This location allows the measurement of high-resonance magnetic field oscillations.

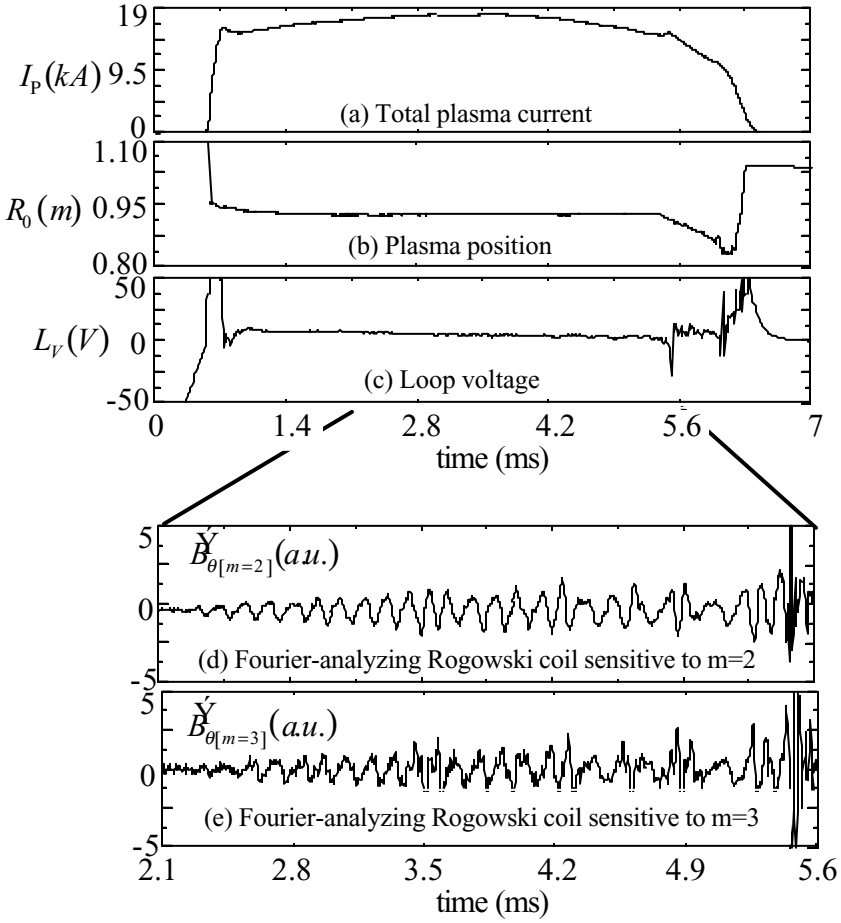

Fig 5.1 Typical HBT-EP measurements from shot # 8817

4.2 Soft x-ray array

The soft x-ray flux is a function of electron temperature, electron density and effective charge. Therefore, soft x-ray diagnostics are sensitive to changes in these quantities and their small fluctuations can be easily detected. This together with magnetic perturbation diagnostics, allow the study of MHD instabilities.

One of the more useful diagnostics on HBT-EP is the sixteen channel array of XUV photodiodes. This array provides profile information. A sketch of its mechanical assembly inside the vacuum chamber port is shown in Fig 4.2.

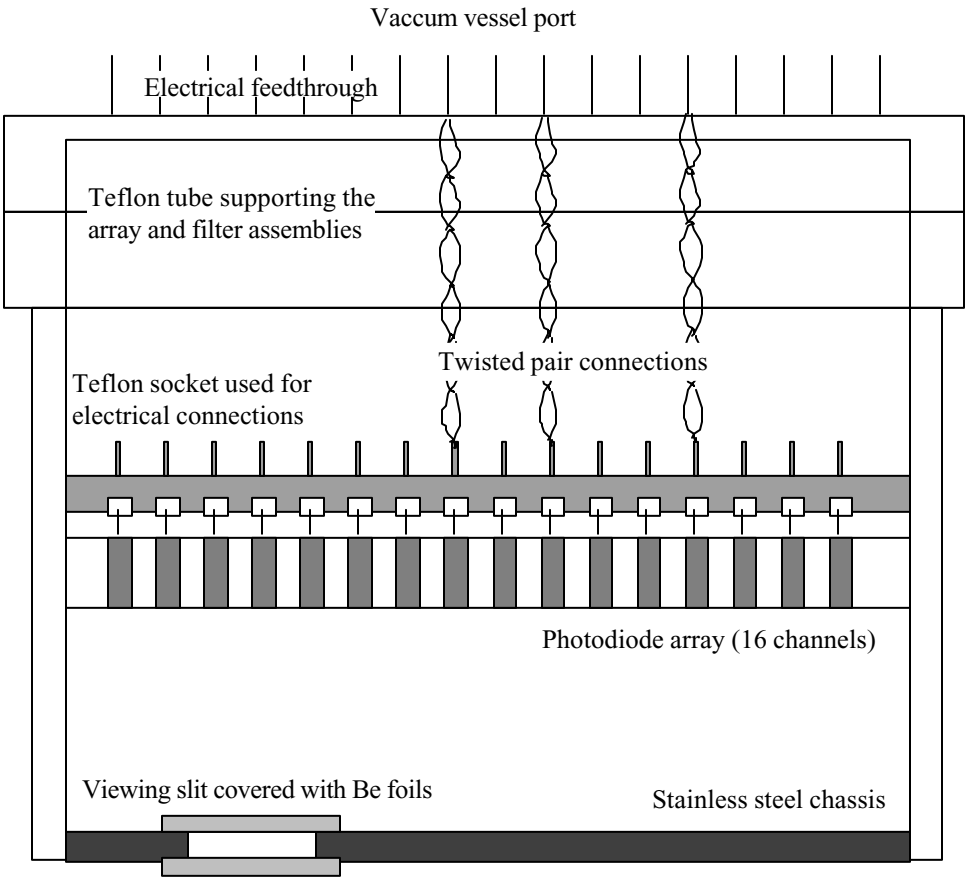

Fig 5.2 Sketch of the 16 channel photodiode array assembly inside the vacuum chamber port

4.2.1 The detectors

The detectors are silicon p-n junction XUV photodiodes with an energy range from $7eV$ to $6000eV$ manufactured by International Radiation Detector (IRD). Each of the devices has an active area of $10\ mm^2$ $(2\ mm \times 5\ mm)$, a low capacitance on the order of $100\,pF$ and a response time of $0.5\mu s$. The diodes are mounted in series on a ceramic chip package $(5.3\ cm \times 2\ \text{cm})$ with a $0.5\ mm$ separation between them thus creating an

array of sixteen channels. Each channel is electrically connected to two opposing pins on the package. The four corner pins on the chip represent the anode (connected to ground in our case). The IRD part number for this chip is AXUV-16LO.

When a photodiode is exposed to photons of energy greater than 1.12 eV (wavelength less than 1100nm), electron-hole pairs (*carriers*) are created. These photogenerated carriers are only separated by the p-n junction electric field, thus a current proportional to the number of electron-hole pairs created can flow through an external circuit. Unlike common p-n junction diodes, these devices do not have a doped dead-region and have zero surface recombination resulting in very high quantum efficiencies (electrons seen by external circuit per incident photon). The output can be predicted in most of the XUV region by the theoretical expression $E_{ph}/3.63$ where E_{ph} is photon energy in electron-volts (eV) [5]. Also, these XUV diodes are internal photoelectric devices and hence are not very sensitive to minute vacuum system contaminants that usually affect conventional XUV detectors based on the external photoelectric effect. Therefore, the photodiode array can be placed inside the vacuum and operated without added difficulties.

4.2.2 Beryllium filter and photodiode response

In order to *blind* the devices to visible light and limit their energy range to that of soft x-rays, a Beryllium filter assembly is used between the detectors and the plasma. The assembly consists of a stainless steel round chassis with a slit in it and Beryllium foils. The chassis was machined at Columbia and later sent to ACF Metals where two Beryllium foils, each 200 *nm* thick, were epoxied on the stainless steel.

The Beryllium foils, fragile as they are, are reinforced with an ultra-thin non-obstructing mesh. The two foils are mounted in series on each side of the chassis thus bringing the effective thickness of the Beryllium between the plasma and the detectors to 400 *nm* . Figure 4.3 shows the calculated transmission of a Beryllium film, 400 *nm* thick, for photons in the X-UV and soft x-ray range. This was carried out using data tabulated by Henke *et al* [6] for thin film transmissions calculated from photoabsorption cross sections. Beryllium bulk density was taken to be $1.85\, g \cdot cm^{-3}$ and Beryllium $K_{edge} = 111eV$ was assumed. The filter assembly makes the devices most sensitive to plasma soft x-ray emission radiation in the energy range from $40\, eV$ to $111eV$.

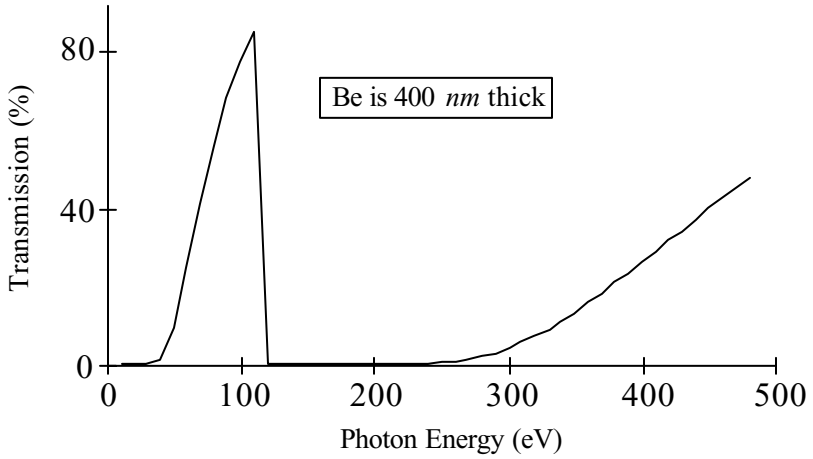

Fig 4.3 Berylium transmission response to photon energy

The relative response of the photodiodes viewing the plasma through the Beryllium filter to different temperatures has also been calculated. Only bremsstrahlung and recombination radiation were taken into account in the computation. A theoretical quantum efficiency of one electron-hole pair per 3.63 eV photons was assumed for the

photodiodes. The calculated Beryllium transmission was then combined with the theoretical quantum efficiency to get the response of the detector-filter assembly. Figure 4.4 shows the resulting photo current for detectors using 400 nm and 600 nm thick Beryllium as a function of plasma temperature.

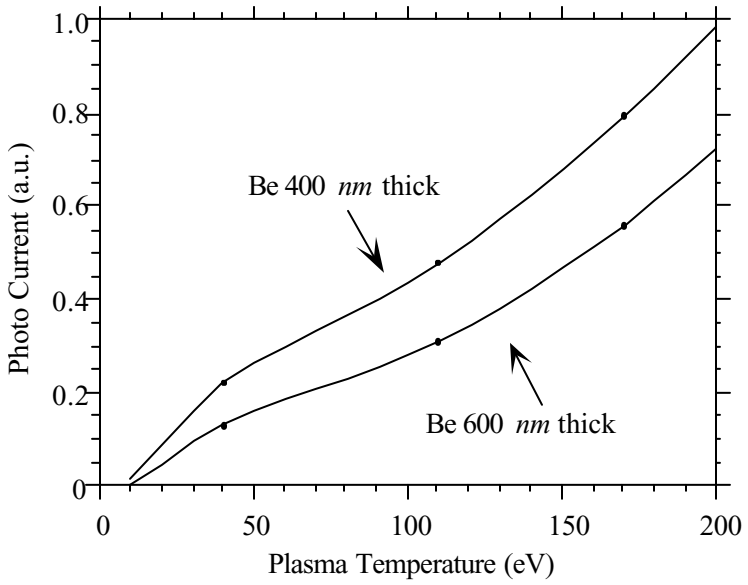

Fig 4.4 Relative response of photodiodes with various thickness Beryllium filters vs plasma temperature

4.2.3 Trans-impedance amplifier

The photodiodes are connected to a vacuum electrical feedthrough with Kaptan insulated wire in a twisted pair configuration to avoid magnetic pick-up (see sketch in Fig 4.2). The signals are then amplified using sixteen trans-impedance amplifiers. A Burr Brown operational amplifier OPA 627 AM (metal package) is employed as the main component of the circuit. It is chosen because of its high bandwidth (10 MHz) and its low input bias current (20 nA). Each amplifier channel is powered individually with a $\pm 12\ V$

power supply for better isolation and to avoid ground loops. All sixteen of these trans-impedance amplifiers have the same gain. The amplified signals are then sampled at 100 KHz using Aurora A-12 digitizers. Figure 4.5 shows a diagram of the circuit.

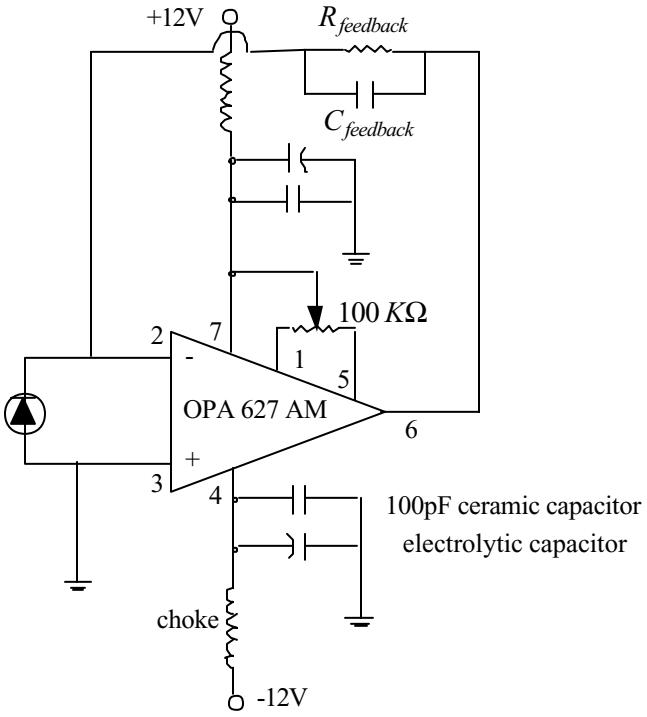

Fig 4.5 Circuit diagram of the trans-impedance amplifier used with the photodiodes

4.2.4 Calibration

The detector-slit assembly was bench calibrated (without the Beryllium filter) using a monochromatic DC light source to exactly map out the geometry of each channel. The specific viewing chords of each detector in the poloidal plane are shown below in

Fig 4.6. The differences due to varying solid angle extents from channel to channel were calculated and taken into account in our signal interpretation.

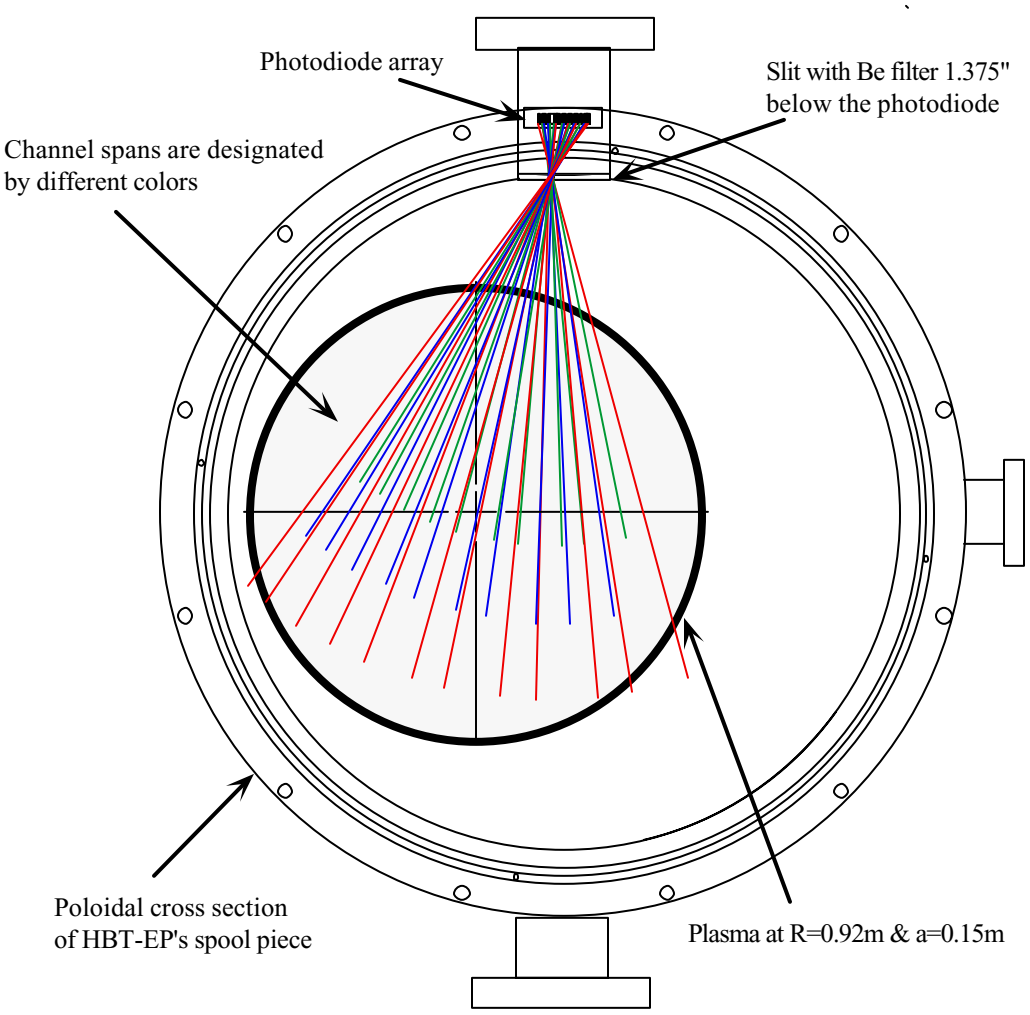

Fig 5.6 Soft x-ray array channel map out

4.2.5 Typical measurements

The signals, once multiplied by the appropriate calibration constants, are plotted either in contour form or just as raw data. Figure 4.7 displays typical soft x-ray plots. In part (a) two chord integrated signals are overlaid. The blue trace is from a plasma-edge

detecting channel and the red are from a plasma-core viewing channel that exhibits periodic thermal crashes known as sawteeth. In part (b), all sixteen channels are used to form a contour plot.

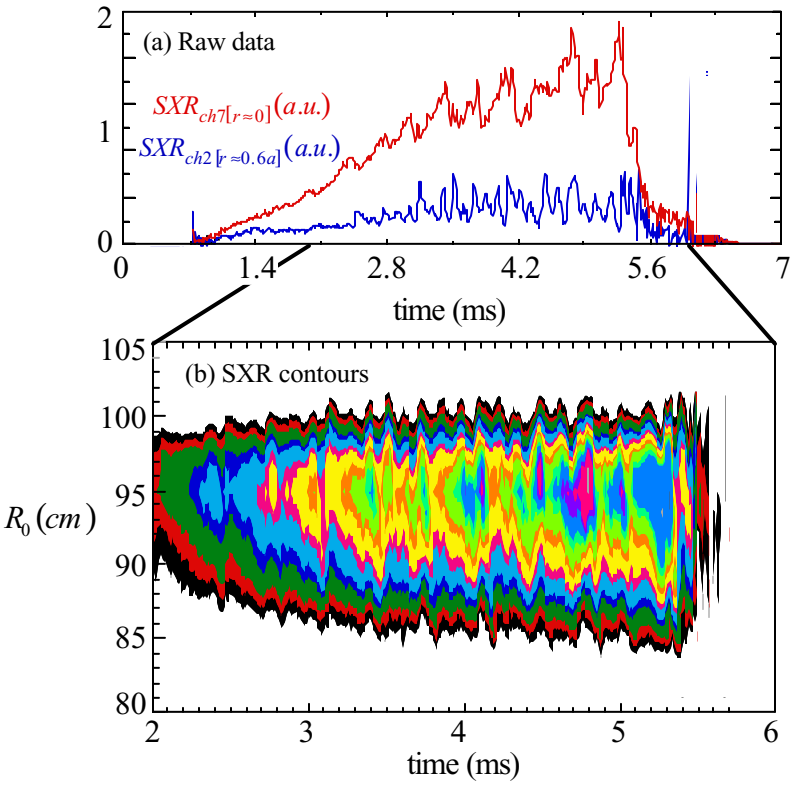

Fig 5.7 Soft x-ray signals for a sawtoothing discharge

4.4 Broad band radiometer

An X-UV100 photodiode manufactured by UDT Sensors Inc. is used to measure total radiated power from the plasma over a broad spectral band. The detector is a silicon p-n junction device developed for use in the X-UV spectral range, i.e. photons with energies between 6 eV and 12 KeV. The photodiode has a high stable quantum efficiency which is predicted by the simple expression $E_{ph}/3.63eV$ [9]. The active area of the device is $1\ cm^2$. Like the soft x-ray array, the photodiode has no external bias applied across it (thus eliminating leakage currents) and the current detected is amplified through

a trans-impedance amplifier similar to the ones used by the array channels (see section 5.2.3). Fig 4.9 shows a diagram of the detector assembly on a spool piece of the vacuum chamber.

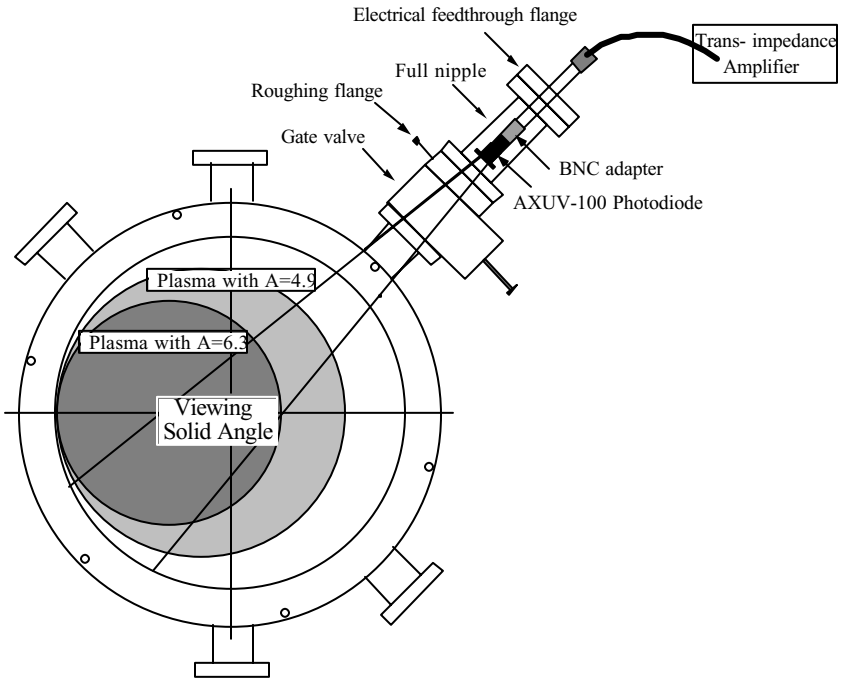

Fig 4.9 Cross section view of spool piece with Radiometer assembly

4.5 Data acquisition

Signals from the various diagnostics (e.g. magnetic probes, Rogowski coils, flux loops, soft x-ray diodes) are recorded by digitizers located in CAMAC crates mounted in shielded racks located around the experiment. Once the data is digitized, it is translated via a fiber optic serial data-link, to a MicroVax 4000-200, where the information is stored on disk. A schematic of the setup is shown in Fig 4.10.

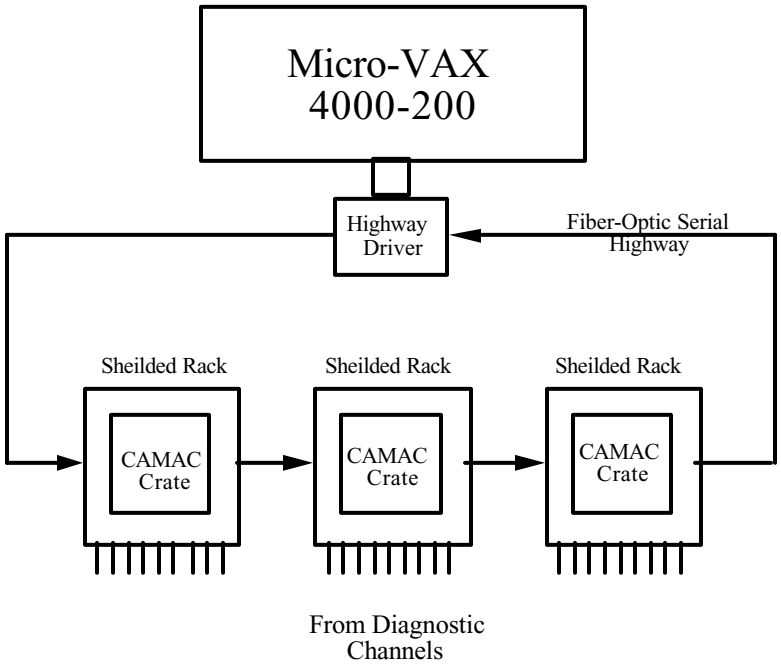

Fig 4.10 Schematic of HBT-EP's data acquisition system

The database management software used is the MDS system developed at MIT. Raw data, calibration data and processed data are all written and stored in different levels of the HBT-EP database.

Reference list:

[1] I.H. Hutchinson, *Principles of Plasma Diagnostics* (Cambridge University press, NY 1987).

[2] H.Y. Che et al., Rev. Sci. Inst. **59** 1057 (1988).

[3] Equipe TFR, Nuc. Fusion **18** 647 (1978).

[4] A. Garofalo, Ph.D. thesis, Columbia University, 1996.

[5] R. Korde et al., SPIE (x-ray instrumentation) **1140** 126 (1989).

[6] B.L. Henke et al., At. Data Nuc. Data Tables **54** 181 (1993).

[7] Q. Xiao and G.A. Navratil, Rev. Sci. Inst. **67** 3334 (1996).

[8] Q. Xiao, Ph.D. thesis, Columbia University, 1997.

[9] L. Canfield et al., Applied Optics **28** 3940 (1989).

[10] F. Chen, *Introduction to Plasma Physics and Controlled Fusion* (Plenum press, NY 1984).

[11] J. Friedberg, *Ideal Magnetohydrodynamics* (Plenum press, NY 1987).

[12] J.C. Hosea et al., Plasma Physics and Controlled Nuclear Fusion Research **1970** IAEA, Madison (1970).

Chapter 5

Soft X-ray Tomography

This chapter describe the hardware of the soft X-ray tomography system on the HBT-EP tokamak. The software part will be described in the next chapter.

5.1 Overview

Measuring the intensity of the soft X-ray emission from the plasma in a is one important means of studying and understanding tokamak characteristics. Various experiments have been performed in which such measurements have been made[1, 2, 3], and soft X-ray detectors have become standard diagnostic equiment on tokamaks.

Soft X-ray emission from tokamak plasmas is dependent on various plasma parameters, such as density and temperature, and one can infer information about them by observing this radiation. This information can then be analyzed and related to propertiies such as plasma position, shape, impurity distribution, and magnetohydrodynamic(MHD) instability phenomena. It is therefore desirable to have as much knowledge of the spatial structure of the soft X-ray emissivity as possible. A plasma in the temperature and density range of interest is optically thin in the soft X-ray region of the spectrum, so the radiation from plasma reaches an externally located detector without much intervention. Thus, with suitably performed measurements, one

can reconstruct the two-dimensional soft x-ray emissivity function in the poloidal cross section of the plasma.

Two soft X-ray system has been designed and built on HBT-EP to study the mode structures of the MHD instabilities. A 16 channels soft X-ray array with a thin berillium filter was built to monitor the m = 1 mode structure. This system was described in the previous chapter. This chapter describes the soft X-ray tomography system. The soft X-ray sysetm consists of 32 channels that are distributed uniformly in both the poloidal and radial directions. The detector system consists of photodiodes with a specially designed thin film filter to cut off lower energy photons. Fig 5.1 is a schematic of the data collection. Soft X-ray photons radiating from the inside of the plasma are collected by the photodiodes through collimators. The photo current is then amplifiered by trans-impedance amplifiers, and then digitized and stored in the database. The following sections will describe each part in more details.

5.2 Photodiodes

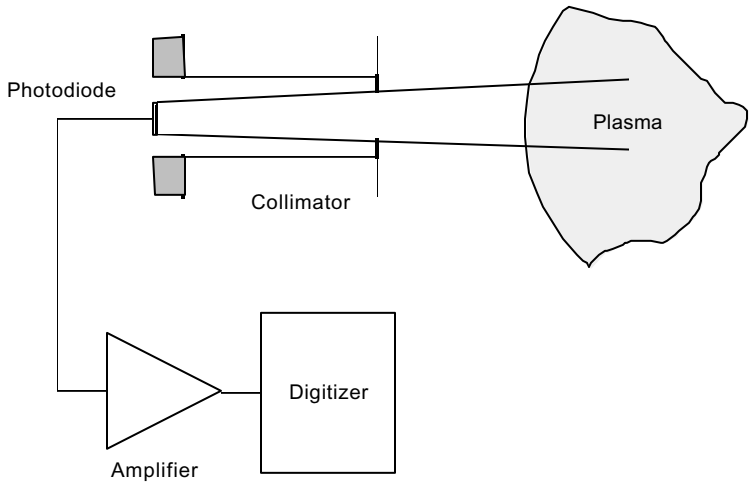

Fig 5.1 Data Collection of Soft X-ray Tomography

The photodiodes chosen are AXUV-20's manufactured by International Radiation Detector Inc.. AXUV-20 has a sensitive area of $20mm^2$, and a capacitance less than 500pF. Since capacitance is a critical factor in the noise perfomance of the detectors, pre-selection of the photodiodes with less capacitance is neceaasry. According to the manucturer, a technique of fabricating a silicon *p-n* junction without creation of a suface "dead region" (no recombination of photo generated carriers in the doped n^+ region, or at the $Si-SiO_2$ interface) was used. Furthermore, the SiO_2 layer was reduced to less than 8mm thickness. Subsequently, these diodes exhibit near theoretical qunatum efficieies for photons with energy from 6 to 6000 eV. Reference [4] gives the details of the fabrication process.

Tests show that a non zero bias voltage produces an unacceptably high dark current (the current from the photodiode when no radiation is incident upon it). Thus, the photodiodes are operated in a non bias mode.

5.3 Filter Design[5]

A high pass filter is needed to filter out lower energy photons. Usually, a seperately surported aluminum or berylium thin film filter is used. The shortcoming of this scheme is that the thin film is very fragil. With low plasma temperatures and densities, the normally thin film has to be even thinner, which is unacceptible. Therefore, we asked the photodiode manucturer to deposit the thin film filters directly on the surface of the photodiodes. Berylium has been commonly used as the filter material. However, since berylium is toxic, we designed a three layer filter consisting of zircomnium, titanium and carbon. In the calculation, the transmission coefficient of a material, f_2, was experimental data taken by B. L. Henke, et al.[6]. The data were downloaded from a Soft X-ray World Wide Web server, http://xray.uu.se/hypertext/henke.html.

The intensity of the radiation as a fuction of the thickness of the filters is

$$\frac{I}{I_0} = \prod^{i} \exp(-\mu_i x_i) \tag{5.1}$$

where I_o is the intensity before the beam enters the material, and I is te intensity in the material. μ_i is calculated from the following equation

$$\mu = 3.39397 \times 10^{11} \frac{\rho \lambda f_2}{A} \tag{5.2}$$

λ is wavelength in cm. ρ is density in $g \bullet cm^{-3}$. A is the atomic number.

The thicknesses of each layer were varied during the calculation to optimize the response. Besides the filter materials, the 8 nm thick of SiO_2 layer on the surface of the photodiode is taken into account. Based on the calculation, a combination of 100nm zrcomnium(Zr), 7.5 nm titanium(Ti) and 100 nm carbon(C) has been chosen. Figure 5.2 shows the calculated transmission of the Zr/Ti/C filter in the X-UV and soft X-ray range.

Relative response of the photodiodes to different temperature plasmas has also been calculated. In the calculation, bremstraulung radiation and recombination radiation have been taken into account. A theoretical quantum efficiency of 3.63 electrons per eV photons has been assumed. The bremstraulung radiation spectrum is: [7]

$$U_{f,T_e} = 6.37 \times 10^{-53} N_e N_i Z^2 (kT_e)^{-1/2} g \exp(-hf / kT_e)(W \bullet m^{-3} \bullet Hz^{-1}) \tag{5.3}$$

in which

$$g = \frac{\sqrt{3}}{\pi} \ln(\frac{4kT_e}{1.78hf}) \tag{5.4}$$

and kT_e is in eV. The recombination radiation spectrum is

$$U_{n,f,T_e} = 1.73 \times 10^{-51} N_i N_e \frac{Z^4}{n^3 (kT_e)^{3/2}} g \exp(-\frac{hf - |E_n|}{kT_e})(W \bullet m^{-3} \bullet Hz^{-1}) \tag{5.5}$$

in which

$$E_n = -Z^2 \frac{\chi_H}{n^2} \tag{5.6}$$

For our calculation, we took into account n = 1, 2 terms.

Figure 5.3 is the calculated relative response of a photodiode with the Zr/Ti/C filter as a function of plasma temperature. In comparison, figure 5.3 also shows the relative responses of photodiodes with a beryllium filter and an aluminum filter as a

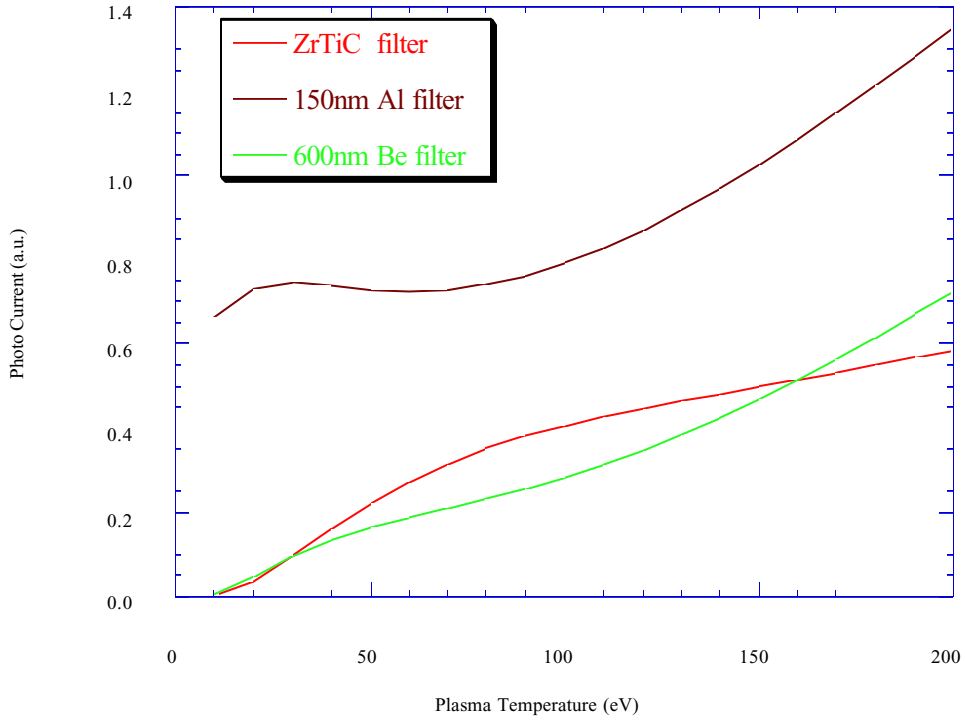

function of plasma temperature.

Fig 5.2 Relative output as functions of plasma temperature for photodiodes with different filters

Fig 5.3 Transmission of the Zr/Ti/C thin film filter(Zr 200nm, Ti 5nm, C 50nm).

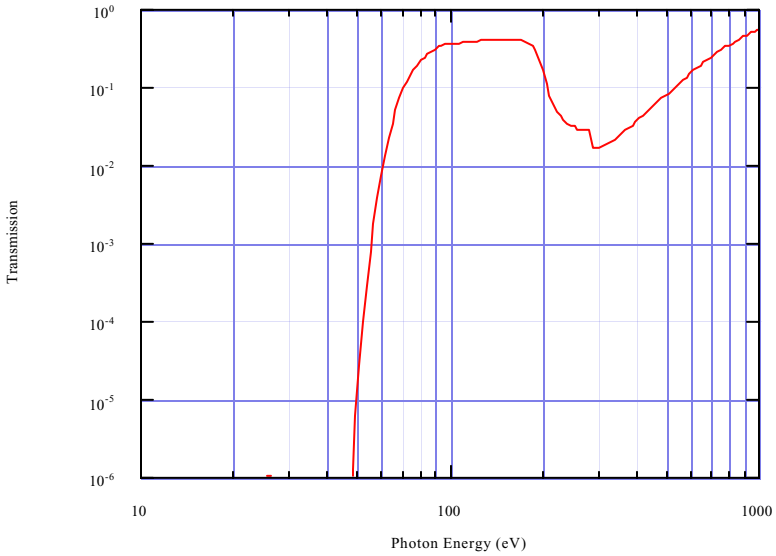

5.4 Detector layout and collimation

Usually tokamak impose strinent space constraints on diagnostics. That's why most tokamaks limit their multi channel soft X-ray systems to one or two poloidal locations. We designed our 16 channel soft X-ray array system in this way. However, this configuration doesn't provide enough poloidal angle coverage for the study of the structure of an m = 2 mode. Tomography algorithms also call for uniform angle distrbution of detectors. This issue will be further addressed in Chapter 6 of this thesis. Fortunately, for the soft X-ray tomogarphy system on HBT-EP, we were able to distribute the 32 channels of detectors uniformly in both poiloidal and radial directions. A vacuum chamber section with 32 viewing ports was built. One detector is attached to each viewing port. As Fig 5.2 shows, the detectors are located at 0^{o}, 45^{o}, 90^{o}, 135^{o}, 180^{o}, 235^{o}, 270^{o}, 315^{o}. The distance between each channel is 4.0 cms. This design allows us to tell the m mode number by looking at phase differences between channels located at the same radial positions but at different poloidal positions.

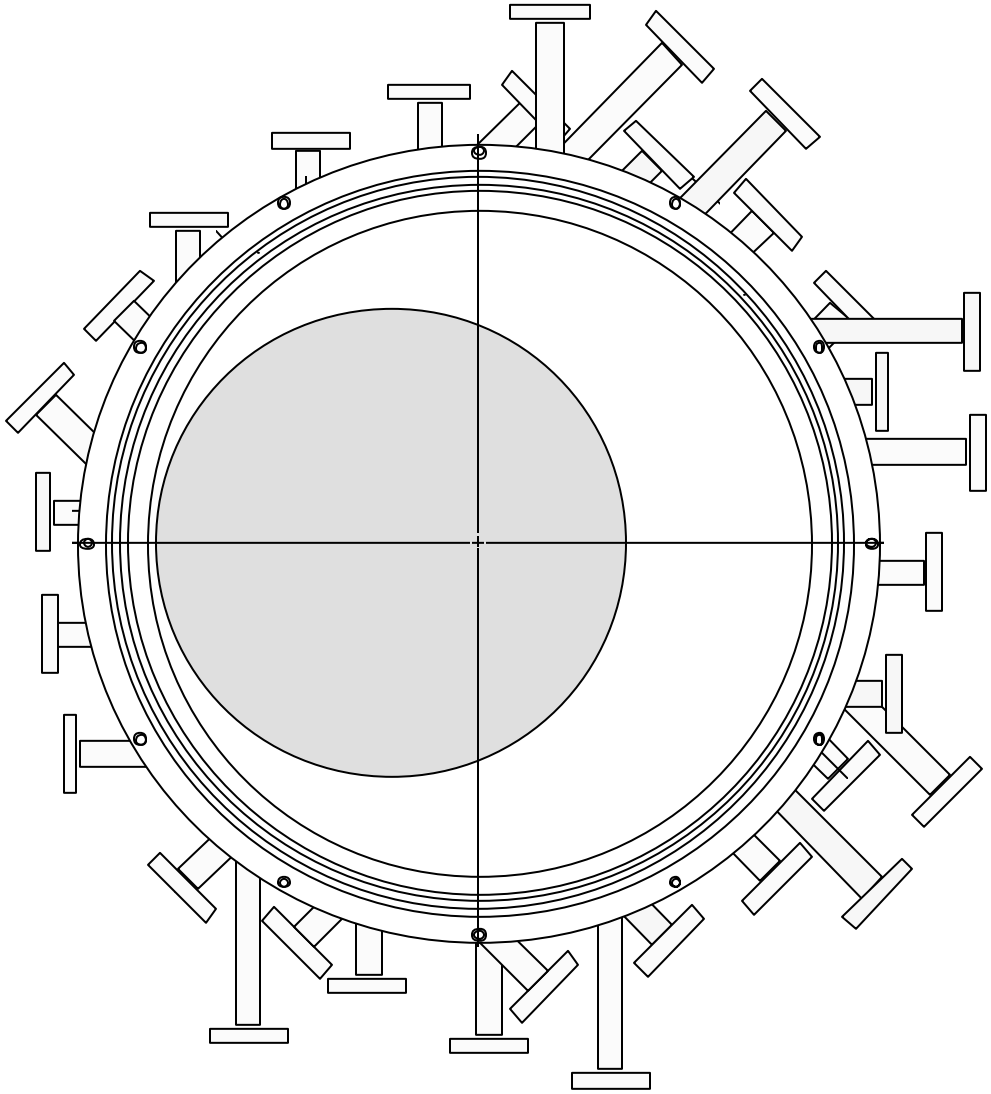

Fig 5.2 Detector layout

The tomography chamber section is made of 316 stainless steel, as shown in Figure 5.6. It consists of two flanges with each flange welded to a stainless tube. A section of bellows were used to connetced the two parts together. This design offesets the error of the dimension and installation of the vacuum chamber. It has a inner diameter 17.5 inches. We used double O-rings for the vacuum sealing between the section and

other ajacent sections. The O-ring groves were designed with a duck-tail shape(not shown) to prevent the O-rings move falling out during installation.

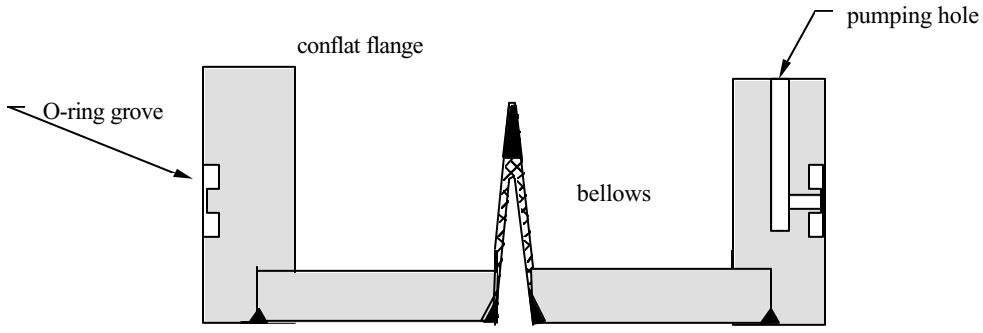

Fig 5.6 Tomography vacuum chmabere section detail

Each viewing port consists of a 2-1/8" stainless steel conflat flange welded to 3/4" diameter tube. The view of each detector is collimated by an aperture with a dimesion of 0.1" in the poloidal direction and 0.5" in the toroidal direction. The collimator is made of alluminum and the phtodiode sits in the middle of it. The collimator is then pluged into a socket made of Teflon which is attached to a 2-1/8" electrical feedthrough flange. The whole assembly is then bolted to the conflat flange of the viewing port.

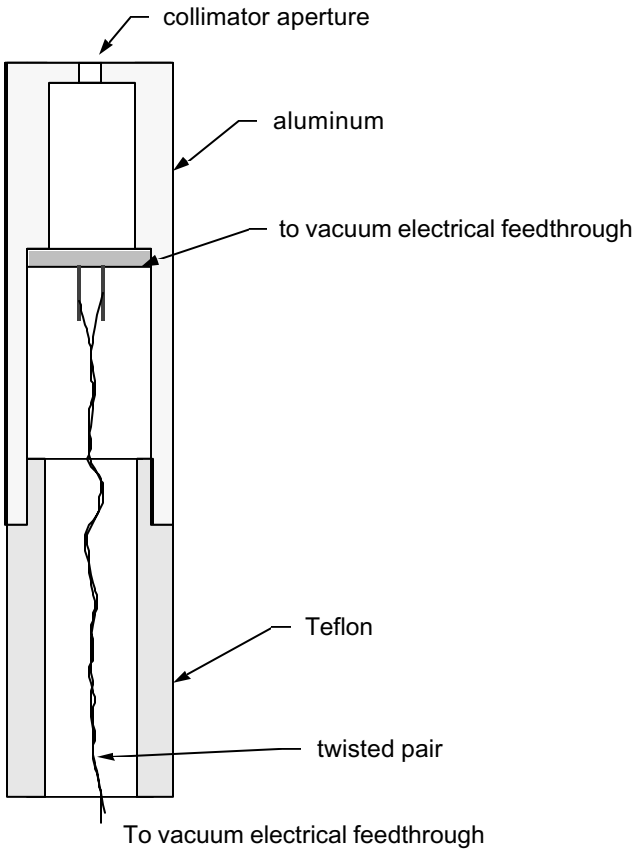

Fig 5.6 Detector Collimator

5.5 Electronics

The photodiodes are connected to a vacuum electrical feedthrough with Kaptan insulated wire in a twisted pair configuration to avoid magnetic pick-up. The signals are then amplified using 32 trans-impedance amplifiers. A Burr-Brown operational amplifier OPA 627AM is employed as the main component of the circuit. It has an low input bias current (about 2 pA), a very low noise level ($4.5nV/Hz^{1/2}$ at 10 kHz). The open-loop output impedance is about 55 ? . We chose the metal can version of the op-amp to

minimize picp-up. The 32 channels of amplifiers are powered by two ±12V power supplys. To reduce the cross-talk between channels, low pass filters were put on the power supply lines of the op-amps. The low pass filters consist of a choke, a electrolytic bypass capacitor and a ceramic bypass capacitor. To further reduce high frequncy noise, a low pass filter with a cut-off frequncy of about 50kHz were used at the output of the amplifiers. All the low pass filters are located in a separate shielded aluninum box, so that it can be disconnected from the circuit easily. Each amplifier channel of has three sets of feedback resisitors and capacitors, so we can use dip switchs on the pc board to select gains. The amplified signals are then sampled at the rate of 100 KHz using Aurora A-12 digitizers. Figure 5.5 shows a diagram of the circuit.

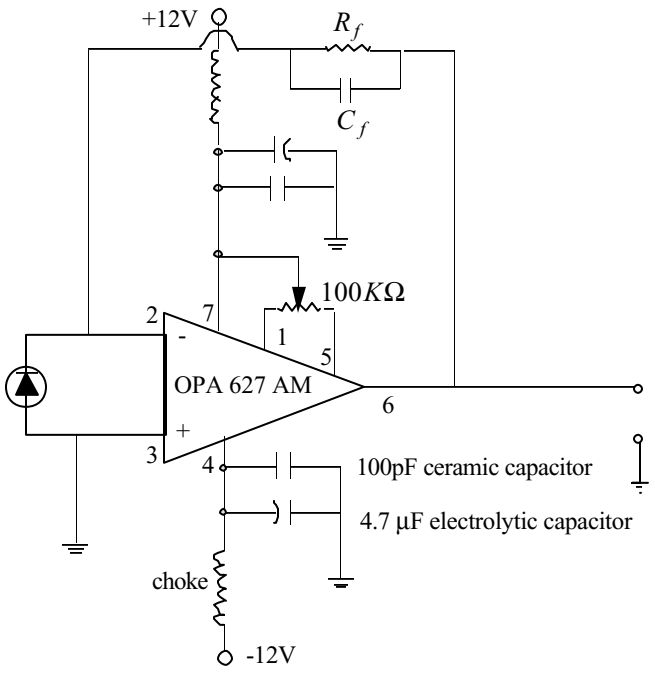

Fig 5.5 Amplifier circuit

A lot of effort went into minimizing amplifier noise, magnetic pickup and electrostatic pickup. The vacuum chamber section itself is grounded to elliminate static pickup. Collimators are made of alluminum to provide shielding. The bandwidth of the amplifiers is limited to 50kHz to cut off high frequency noise. We use twisted pairs to transmit signals, so that the coupling of noise through the transmission line is minimal. Both the amplifiers and the power supply for the amplifiers are housed in a copper box which is grounded. We achiev satisfactory signal capture and noise reduction through these efforts.

Reference list:

[1] S. Von Goeler, et al., Phys. Rev. Lett. **33**, 1201(1974).

[2] J. F. Camacho, et al., Rev. Sci. Instrum., **57(3),** March 1986.

[3] Y. Nagayama, Phys. Plasmas**, 3(7)**, July 1996.

[4] R. Korde, et al., IEEE Trans. Nucl. Sci. **NS-40**, 1655 (1993).

[5] Qingjun Xiao and G. Navratil, Rev. Sci. Inst. **67**, 3334 (1996).

[6] B. L. Henke, E. M. Gullikson, and J. C. Davis, Atomic Data and Nuclear Data Tables, Vol. 54, No. 2(1993).

[7] Z. Xiang and C. Yu, High Temperature Plasma Diagnostics, Shanghai Science and technology Press, (1984)

Chapter 6

Data Analysis Methods

This chapter describes the methods of data analysis for extracting information from the soft X-ray signals. In section 6.2, I describe the Fourier tomography algorithm and give details of the implemantation. Section 6.3 talks about the Maximum Entropy algorithm. I describe the algorithm and give a brief commentary on this method. A way of plotting the soft X-ray signals to show the plasma rotation is also presented here.

6.1 Oerview of Tomography Algorithms

In plasma diagnostics, radiation measurements are made outside the plasma. An inversion technique is required to reconstruct the plasma image from the line-integrated measurements. When the plasma is cylindrically symetric, Abel inversion is used to obtain the radial distribution. However, in most cases, the distribution is not cylindrically symetric, and most imporatant, we need to extract more information than just a simple radial distribution from the radiation measurements. A kind of computational tomography has become necessary to obtain the plasma image. Tomography techniques are well developed in the medical diagnostics, but it is difficulty to apply those same techiniques to a plasma diagnostic, because as a plasma diagnostic the number of detector arrays is much less, and the noise is much higher than in medical applications. Thse problems can be overcome by using the fact that the structure of a plasma is much simpler than that of a human organ.

The response of each detector is a volume integral of the plasma emissivity weighted by a weight function over the entire plasma. It can be given by the following equation:

$$I_i = \iiint_{plasma} g(x,y,z) w_i(x,y,z) dxdydz$$

g(x, y, z) is the emissivity, and w_i *(x, y, z)* is the weight function for detector i. The problem of tomography is to reconstruct *g(x, y, z)* from the measured I_i. The algorithms used in a tokamak application include the Fourier-Cormack method([1, 2, 3]), an maximum entropy algorithm([4]) and an algebraic reiteration method([5]).

The Fourier-Cormack method[1] is prefered to reconstruct MHD mode structure by sevral tokamak groups[2, 3]. It has the advantage of minimizing errors by doing least-squares fitting in orthogonal expansions. The maximum entropy method[4] doesn't assume a limited number of Fourier harmonics. It gives the most probable radiation distribution. In this chapter, I will review these two methods in detail.

6.2 Fourier Algorithm

The concept of the Fourier method is the following. The distribution of emmisisvity is represented by a series of particular functions. The the detected signals can be represented by the series of integrated functions in the line of sight. The coefficients of expansion are found by doing a least-square fit to a series of line-integrated functions to the data. Then an emmisisvity profile can be obtained from the limited number of detectors. Two types of functions for radial expansions are usually used. They are Zernicke polynomials and Bessel functions.

6.2.1 Principle of the Algorithm

First, I discuss the reconstruction technique using least-square fitting in orthogonal expansions. The problem is to determine the emmissivity *g*, from the projection function *f*. We use polar coordinates. The coordinate system is shown in Figure 6.1. So

$$f_i = \int_S g(r,\theta) * w_i(r,\theta) ds \,. \tag{6.1}$$

Here, we suppose that the emissivity is confined to a unit circle and is zero outside the circle. The values of the weight function are numerically calculated, then stored in a file. It is defined as thesolid angle that can be seen by the photodiode. It is a function of radius and poloidal angle, as we have already integrate in the toroidal direction. The weight function calculation will be explained in more detail in the section 6.2.3. The result is loaded in for the rest of the computation during run time.

Let us expand the emissivity function in a Fourier series in θ, and an arbitary series in r:

$$g(r,\theta) = \sum_{m=0}^{\infty} \sum_{l=0}^{\infty} [a_m^{(c)l} \cos m\theta + a_m^{(s)l} \sin m\theta] g_m^{l(r)}. \tag{6.2}$$

We obtain

$$f_i = \sum_{m=0}^{\infty} \sum_{l=0}^{\infty} [a_m^{(c)l} f_{i,m}^{(c)l} + a_m^{(s)l} f_{i,m}^{(s)l}], \tag{6.3}$$

where

$$f_{i,m}^{(c,s)l} = \int_{cross\,section} (\cos m\theta, \sin m\theta) g_m^l(r) * w_i(r,\theta)\, ds. \tag{6.4}$$

When each Fourier component $g_m(r)$ of the source function $g(r, \theta)$ is represented bu a series of particular functions $g_m^l(r)$, the detected signals can be represented bu a series of

functions $f_m^{(c,s)l}$. The coefficients $a_m^{(c,s)l}$ are found by doing a least-square fit of equation 6.3 to the data.

We can further simplify by assuming that the detectors are all uniform, that they are all located infinitely far away and that the field of view is narrow. Then each channel can be indexed using the angle and radial location of the channel, as figure 6.1. In the Cormack inversion, the Zernicke polynomial $R_m^l(r)$ is employed for $g_m^l(r)$ as

$$g_m^l(r) = (m + 2l + 1) R_m^l(r), \tag{6.5}$$

where $R_m^l(r)$ is defined as

$$R_m^l(r) = \sum_{k=0}^{l} \frac{(-1)^k (m + 2l - k) r^{m+2l-2k}}{k!(m + l - k)!(l - k)!} . \tag{6.6}$$

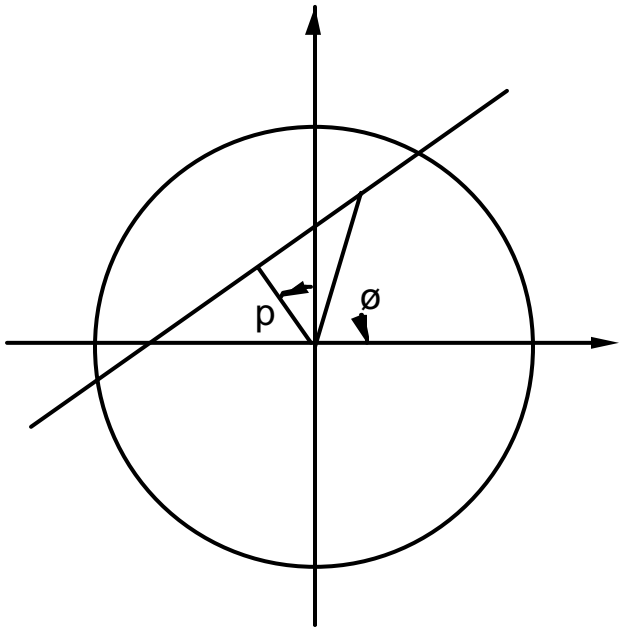

Fig 6.1 Detector coordinate system

Then equation 6.4 becomes

$$f_m^{(c,s)}(p,\phi) = (\cos m\phi, \sin m\phi) 2\sin[(m+2l+1)\cos^{-1} p]. \qquad (6.7)$$

Since the Fourier component $f_m(p,\phi)$ has a simple analytical form, the Cormack inversion is preferred.

One of the problems with the Zernicke inversion is that the Zernicke polynomial is not zero at the boundary. As we know, the source function is zero outside the plasma. Another problem is that we need to assume the field of view of the detector is colimated to a infinitely narrow cylinder. This constraint is too stringent in most cases. After analyzing the difficulties, we took a different approach.

We can represent the source function *g(r, θ)* by the use of Fourier-Bessel expansions.

Also instead of assuming infinitely narrow collimation, we take full consideration of the weight functions for each channels. The following two-sub sections will explore our approach in more detail.

6.2.2 Bessel functions

We represent the emissivity function *g(r, θ)* by the use of Bessel functions for the radial harmonics:

$$g_m^l(r) = J_m(\lambda_m^{l+1} r) \qquad (6.5)$$

l	$j_{0,l}$	$j_{1,l}$	$j_{2,l}$	$j_{3,l}$	$j_{4,l}$
0	2.40483	3.83171	5.13562	6.38016	7.58834
1	5.52007	7.01558	8.41724	9.76102	11.06471
2	8.65372	10.17347	11.61984	13.01520	14.37254

3	11.79153	13.32369	14.79595	16.22347	17.61597
4	14.93091	16.47063	17.95982	19.40941	20.92693
5	18.07106	19.61586	21.11700	22.58273	24.01902
6	21.21164	22.76008	24.27011	25.74817	27.19909
7	24.35247	25.90367	27.42057	28.90835	30.37101
8	27.49348	29.04683	30.56920	32.06485	33.53714
9	30.63401	32.18968	33.71652	35.21867	36.69900
10	33.77582	35.33231	36.86286	38.37047	39.85762
11	36.91710	38.47477	40.00844	41.52072	43.01374
12	40.05843	41.61709	43.15345	44.66974	46.16785
13	43.19980	44.75932	46.29800	47.81779	49.32036
14	46.34119	47.90146	49.44216	50.96503	52.47155
15	49.48261	51.04353	52.58602	54.11162	55.62165

Table 6.1 Zeroes of Bessel functions

where λ_m^l is the lth zero of the mth order Bessel function $J_m(z)$. $f_{i,m}^{(c,s)l}$ is obtained by doing numerical integration of equation (6.4). Zeros of the Bessel functions can either be calculated or looked up in a math table such as [6]. Zeroes for Bessel functions of m up to 4 and l up to 15 are listed in table 6.1. They are stored in a file and loaded during run time.

6.2.3 Weight Functions

We took full consideration of the weight functions into account. Fig 6.2 is

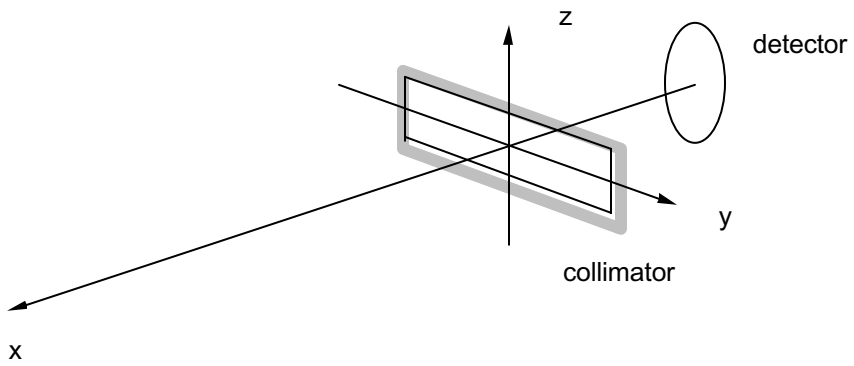

Fig. 6.2 Detector-collimator coordinate system

the coordinate system for the weight function calculation in which y points to the y toroidal direction. The collimator has a rectangular shape with a dimension of 0.5" in toroidal direction and 0.1" in poloidal direction.

We denote A(x,y,z) as a point in the plasma. O is the center of the detector. Projection of the surface of the detector along OA onto the aperture plane is also a circle. We use S to denote the overlap between the projection circle and the aperture. The value of weight function for point A(x,y,z) is then the solid angle subtended by S seen at A(x,y,z). Since the plasma is uniform along toroidal direction, we integrate the weight function along the y direction and store the integrated value onto disk.

Let's use $O_1(x_{o1}, y_{o1}, z_{o1})$ to denote the center of the projection, and $A_i(0, y_i, z_i)$ to denote a point on the aperture plane. The y direction integrated weight function for a point A(x,y,z) is then:

$$w(x,y,z) = \int_y \left(\int_S \frac{\cos\theta}{x^2 + (y-y_i)^2 + (z-z_i)^2} dS \right) dy \qquad (6.6)$$

where $\cos\theta$ is

$$\cos\theta = \frac{x}{\sqrt{x^2 + (y-y_i)^2 + (z-z_i)^2}} \qquad (6.7)$$

The double integration on the aperture plane is done by dividing the aperture into pixels and adding the contribution of each pixel together. If the pixel falls out of the detector projection circle, its contribution is set to zero. The integration along the toroidal direction is done by using the Romberg algorithm. The result of the weight function calculation is stored in a file, and loaded into memory before reconstrunction.

6.2.4 Phantom Reconsctructions:

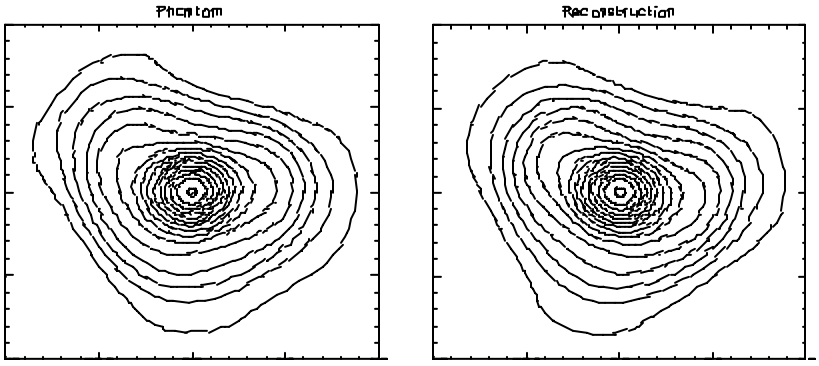

Fig. 6.3 Phantom Reconstruction

The numerical test consists of specifying the emission function over the observed volumn, computing via numerical integration the expected signals on each projection channel, then using the computed projections as inputs to the reconstrcution algorithm, and finally comparing the reconstructed emission function with the one originally specified. Fig. 6.3 shows a comparison between a numercal phantom and the reconstructed image.

6.2.5 Truncation of Fourier Harmonics and Rotation Assumpation

Tokamak is a very difficult enviorment for tomography. We can have only a very limited number of channels, while any reconstruction code needs as many channels of signal as possible. Truncation of Fourier harmonics is necessary. It is also desired, since it is impraticle to use too many Fourier harmonics.

On the other hand, a tokamak is equiped with a lot of other diagnostics. Also some of the physical phonomenon reasonably well understood. We can incorporate this known information into our reconstruction code.

For example, if we already know the dominant poloidal mode number of the MHD structure from another diagnostics, we can use that harmonic together with a m = 0 harmonic to get the structure of that particular mode.

Another common assumption is the mode rotation assumption[2]. If we already know that the mode is rotating rigidly, we can assume we have several identical sets of detectors located at different poloidal angles, we can then use outputs at other time as the data for these rotated channels. We then proceed with the reconstrcuctions using both the real and rotated channels. This way we can take into account of all the available information. We used both of the above techniques in our reconstruction.

6.3 Maximum Entropy Method

We have also tried using the Maximum Entropy Algorithm in our reconstructions. This method is a modified version of a general procedure first outlined by B. Roy Frieden[7]. It was first used in a tokamak at the Columbia Plasma Physics Lab[4]. This procedure consists of a maximum entropy approach to tomographic reconstruction. The most important characteristic is the capability of reconstructing asymmetric density

distributions without any symmetry assumptiions. The algorithm produces the most probable density distribution, smoothed to the cell size.

As shown in Fig. 6.4, we divide emitting region into NC cells (or Pixels). The emmisivity function is then:

$$E(r,z) -> \{E_C\}, \tag{6.7}$$

where c is the index of the cells. We define the quantized emmisivity as:

$$E_C = n_c \Delta E \tag{6.8}$$

where ΔE is an arbitrary number. We then define a quantity called entropy in analogy to the entropy in statistic physics:

$$\Omega_e = -\sum_{c=1}^{NC} E_c \ln(E_c). \tag{6.9}$$

We then maximize the entropy with respect to the following constraints:

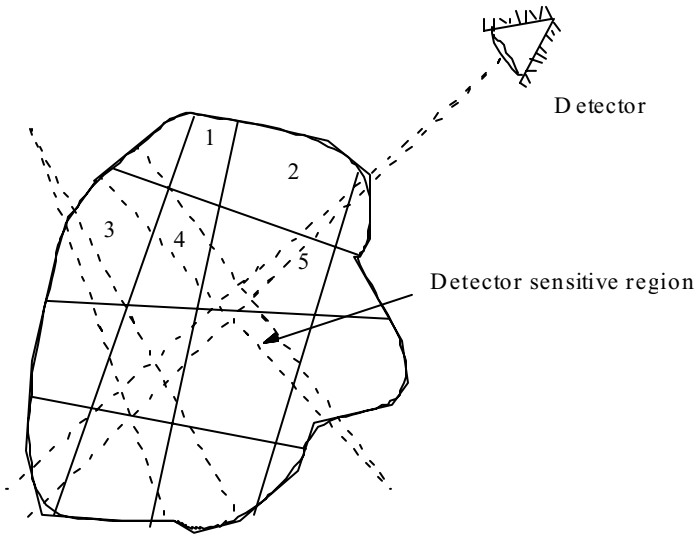

Fig. 6.4 Dividing Emission Area for Maximum Entropy Algorithm

- Total emmision constraint:

$$F_0 \equiv \sum_{c=1}^{NC} E_c - I_0 = 0 \tag{6.10}$$

- Projection constraints:

$$Fp \equiv \sum_{c=1}^{NC} E_c S_{pc} - I_p = 0, 0 < p < NP + 1 \tag{6.11}$$

where S_{pc} is the weight function defined by:

$$S_{pc} = \int \frac{\omega_p(r,z,y)}{4\pi} dV_c \,. \tag{6.12}$$

The way to do the maximization is Lagrangian Multiplier Method. Define:

$$L \equiv \Omega_e + \lambda_0 F_0 + \sum_{p=1}^{NC} \lambda_p F_p$$

$$= -\sum_{c=1}^{NC} E_c \ln(E_c) + \lambda_0 [\sum_{c=1}^{NC} E_c - I_0] + \sum_{p=1}^{NP} \lambda_p [\sum_{c=1}^{NC} E_c S_{pc} - I_p] \,. \tag{6.13}$$

We the solve the following equations for E_c and S_{pc}:

$$\frac{\partial L}{\partial E_c} = 0, 1 \le c \le NC, \tag{6.14}$$

and

$$F_p = 0, 0 \le p \le NP \,. \tag{6.15}$$

References

[1] A. M. Cormack, J. Appl. Phys. **35**, 2908 (1964)

[2] Y. Nagayama, J. Appl. Phys. **62**, 2702 (1987)

[3] R. S. Granetz and J. F. Camacho, Nucl. Fusion **25**, 727 (1985)

[4] A. Holland and G. Navratil, Rev. Sci. Instrum., **57(8)**, (1986)

[5] M. A. Viergever, NATO ASI Series, F39, Mathematics and Computer science in Medical Imaging, edited by M. A. Viergever and A. E. Todd-Pokropek, 1988

[6] F. W. J. Olver, Bessel Functions, Part III, Royal Society Mathematical Tables, **7**, (1960)

[7] B. Roy Frieden, J. Opt. Soc. Am. **62**, 511 (1972)

Chapter 7

MHD Mode Structure Measurement

Extensive study has been carried out on HBT-EP to try to understand MHD mode structures and the interaction between applied resonant magnetic field and the MHD modes. In this chapter I will present mode measurement in a shell inserted discharge. The results of mode measurements in applied resonant magnetic field experiments will also be presented.

7.1 Mode Structure in Shell-stabilized Discharges

The results of wall stabilization of external kink modes on HBT-EP will be briefly summarized in 7.1.1. Mode structure of the "residual" instabilities in the wall inserted discharges will be presented in 7.1.2.

7.1.1 Wall Stabilization of External Kink Mode [1, 3]

In shell studies on HBT-EP, two types of discharges were chosen to illustrate conducting wall effects on the stability and disruptivity of the plasma. In the first category, designated "current-ramp" discharges, plasmas were formed with a prescribed gradual current ramp of $dI_P/dt \approx 6\,MA/s$ to induce a broad current profile with enhanced edge currents known to excite external kinks. The other type of plasmas, designated "rapid formation" discharges, were created using a fast startup with a $dI_P/dt \approx 100\,MA/s$

followed by a much slower current ramp to produce plasmas with more peaked profiles and higher values of β_N near the disruptive limit.

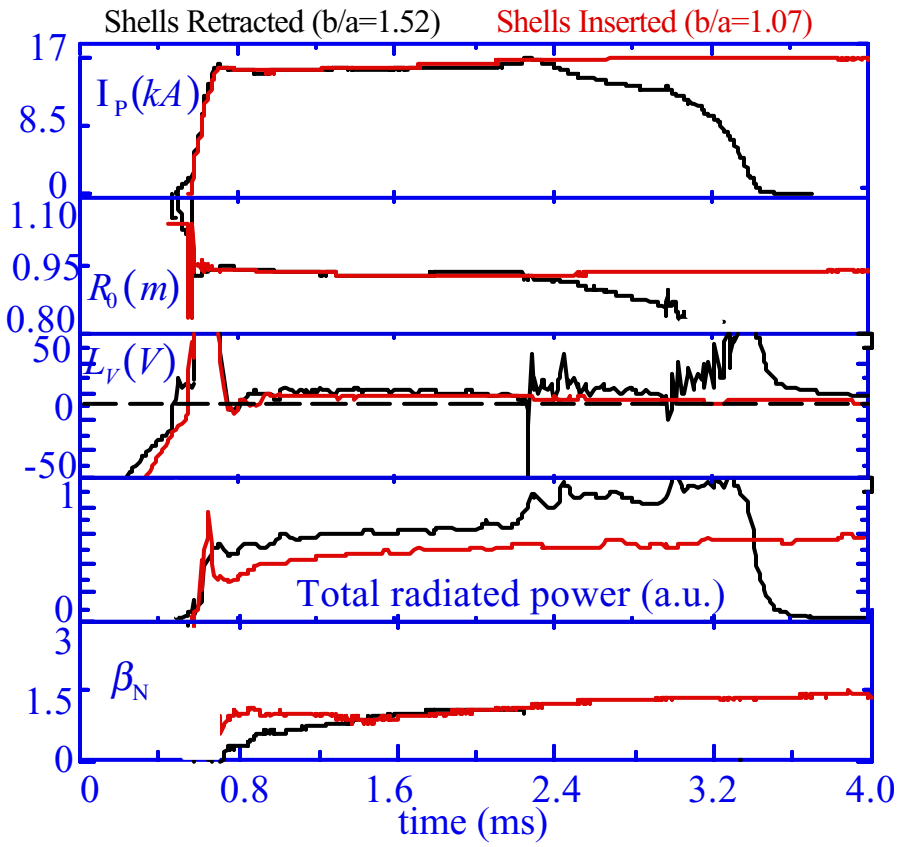

Fig 7.1 Comparison of discharges with the shells inserted and shells retracted

In order to examine the shell effects on these type of discharges, two similarly prepared plasmas were obtained with the shell position being the only difference between them. Figure 7.1 compares the time evolution of the total plasma current, the plasma position, the loop voltage, the total radiated power and the rising β_N for the rapid case, The traces in black are for the plasma with the shells fully retracted (b/a =1.52) and the traces in red are for the plasma with the shells fully inserted (b/a=1.07). The discharges

develop exactly the same way, their global parameters progress at the same rate and are kept as close as possible until $t \sim 2.2$ ms, when the plasma with the shells retracted disrupts as its β_N is reaching the ideal stability limit of 1.5. The plasma with the shells inserted proceeds without any disruptions even as the value of its β_N continues to rise with the modestly increasing plasma current.

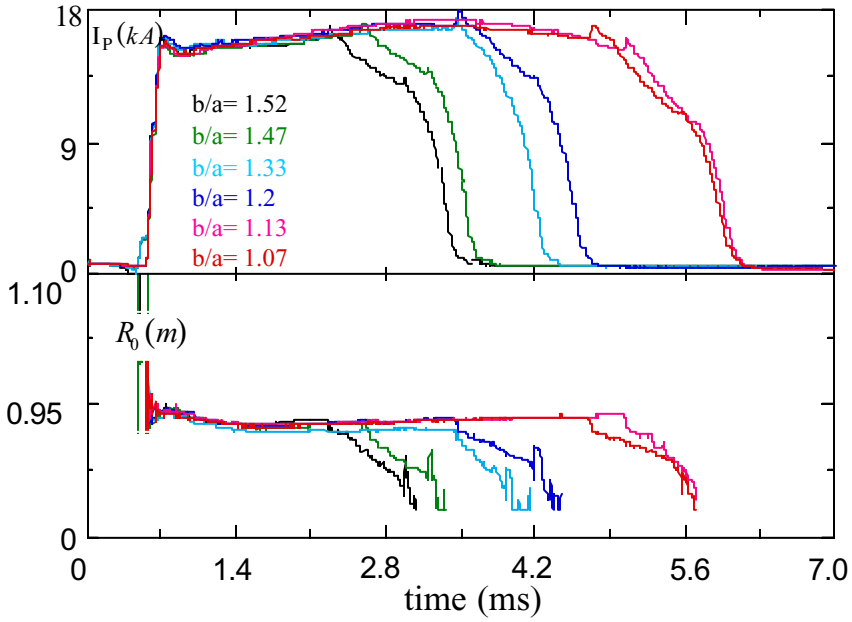

Fig 7.2 Shell scan showing total plasma current and positions as b/a=1.52 is incrementally changed to b/a=1.07.

Figure 7.2 shows the time evolution of the total plasma current and position for a shell scan obtained for rapid formation discharges. The plasmas are similar except for the position of the conducting wall which was varied systematically in 2 cm increments. With the shells retracted, the plasma disrupted as $\beta_N \approx 1.5$ and its disruption mechanism was examined earlier. One immediate observation is the orderly extension of the pulse length or plasma lifetime as the shells are moved closer to the plasma. The improvement

is at least by a factor two. The point is that with the shells retracted a β-limiting disruption terminates the plasma where as for the shells inserted this disruption is avoided. The current ramp discharge presents the same result. It is also evident from the total plasma current traces that the wall-stabilized discharges disrupt during the current ramp-down phase of the discharge.

7.1.2 Tearing modes in wall-stabilized discharges

Although the segmented conducting wall, when it was positioned sufficiently close to the surface of the plasma, prevented kink instabilities, it did not completely eliminate all the MHD instabilities on HBT-EP. Mirnov coils and soft X-ray measurements detected slowly growing and saturated rotating perturbations in these discharges. The perturbations rotate in the electron drift direction. These instabilities often precede disruptions in the ramp-down($dI_p/dt < 0$) phase of the discharge. Indeed, internal, current-gradient-driven tearing modes, particularly the m= 2, n =1, have long been associated with disruptions in tokamaks[2].

In order to understand the disruptions observed in wall-stabilized discharges (that is discharges in which rapidly growing disruptive instabilities are suppressed by the close-fitting conducting wall), the plasma with b/a=1.07 is examined in some details at the end of its lifetime. Figure 7.3 shows the current-ramp down phase of the discharge as well as the internal fluctuations as detected by the Mirnov coils and soft X-ray system measurements.

In Figure 7.3, the top trace is the plasma current. It starts to ramp down at 4.6 ms. The second trace is the signal of the sin2θ coil, which indicates the amplitude of the m =

2 component of the MHD instability. The third graph is the perturbation part of the soft X-ray signals from the channels that locate at the same radial location r = 10 cm but different poloidal locations. The y axis is the poloidal angle of the viewing line of a channel. The color represents the amplitude of the perturbation. As we can see the mode structure seen by the soft X-ray tomography system is dominated by m = 2 component. Mode rotates in the counter-clockwise direction. The m = 2 mode grows prior to the disruption.

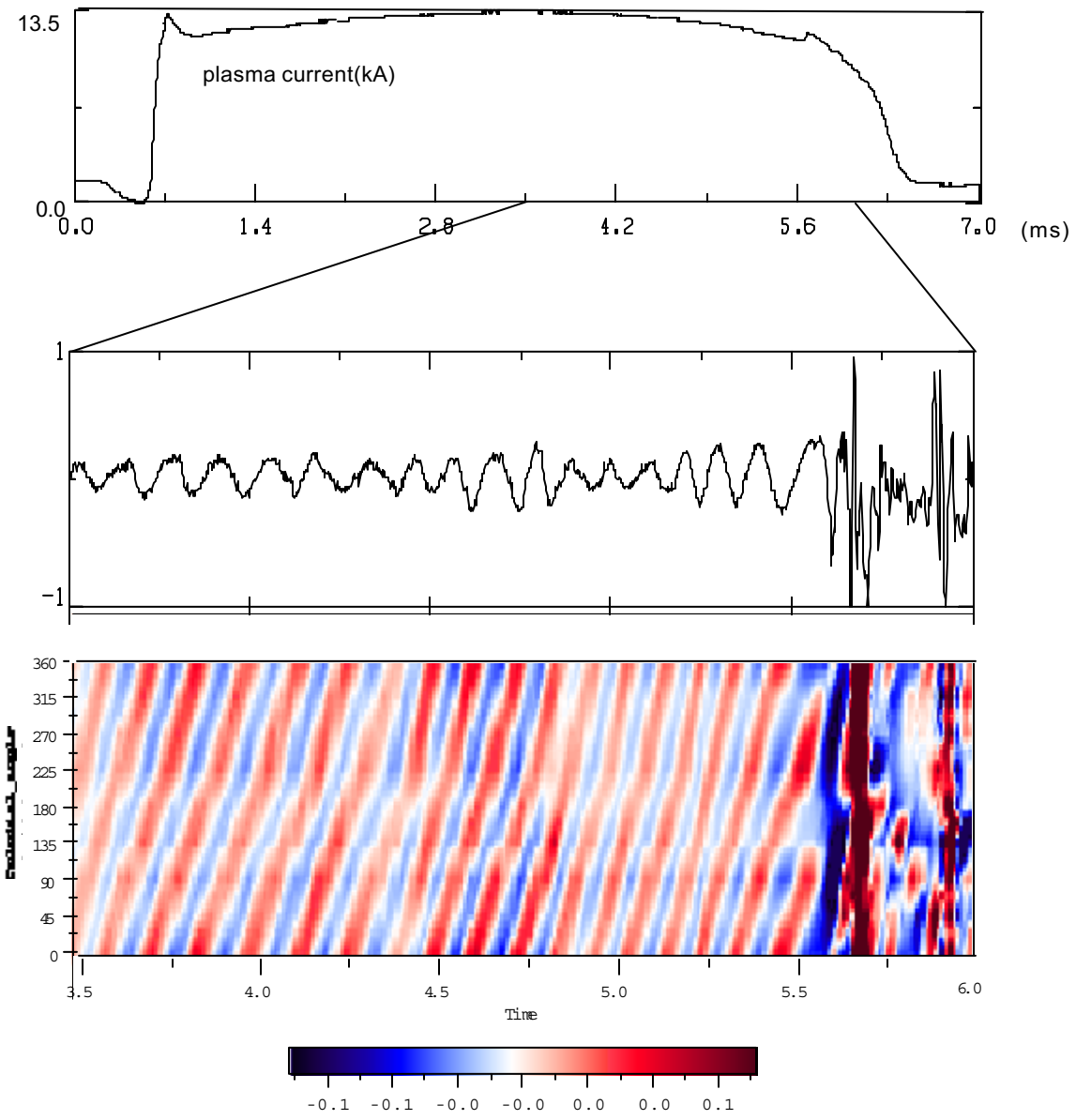

Fig. 7.3 Residual tearing mode in a kink-stabilized plasma

Fig 7.4 is another way of showing the perturbation components of the soft X-ray signals. Each trace is the output of one channel that locates at r = 10 cm. Please see Figure 6.1 for the coordinate system to label the channels. We can see the peaks of oscillations move to different poloidal angle at an later time. The slope indicates the mode traveling speed. By counting the peaks at any time, we can tell the mode number is m = 2.

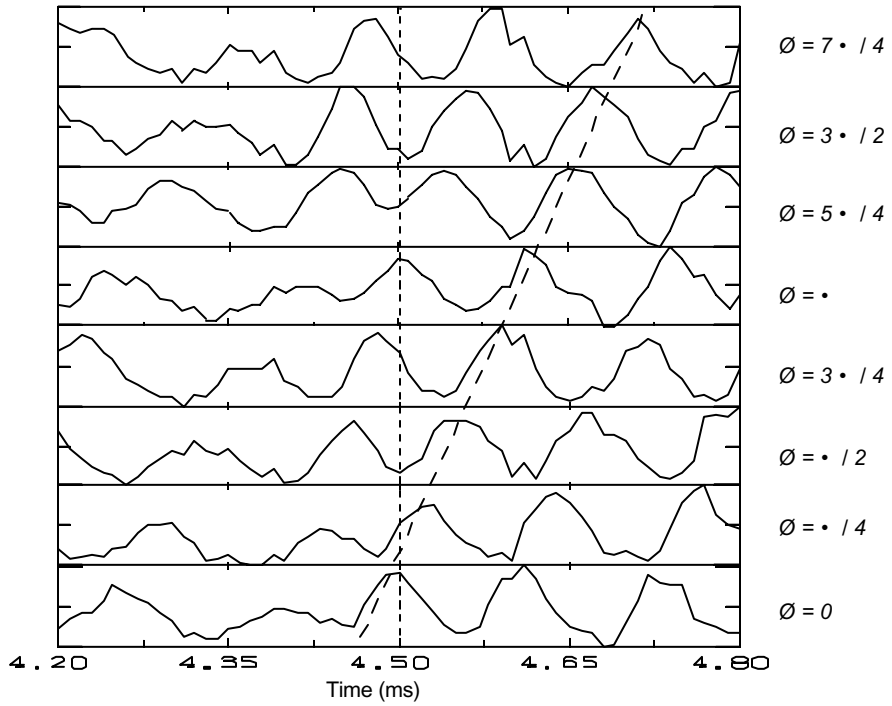

Fig 7.4 Soft X-ray shows m = 2 structure

Fourier algorithm described in the previous chapter was used to reconstruct the soft X-ray radiation emmissivity for these discharges. The reconstruction shows m = 2 island structures. Figure 7.5 is a sequence of contour plots of the reconstruction in half a cycle. The inner dotted lines are the locations of the q = 2

surface. The reconstruction shows m = 2 island-shaped structures at q = 2 surface. In the reconstruction, a rigid toroidal rotation was assumed. The rotation frequency is 8.3 kHz. Two additional sets of detectors are assumed. So we have in total 96 data points at any time. Channel 33-64 are channel 1-32 that are poloidally 60 degree counter-clock shifted, and the data of these channels are the data 0.04 ms earlier of channel 1-32. Channel 35-96 are channel 1-32 that are poloidally 120 degree counter-clock shifted, and the data of these channels are the data 0.04 ms earlier of channel 1-32.

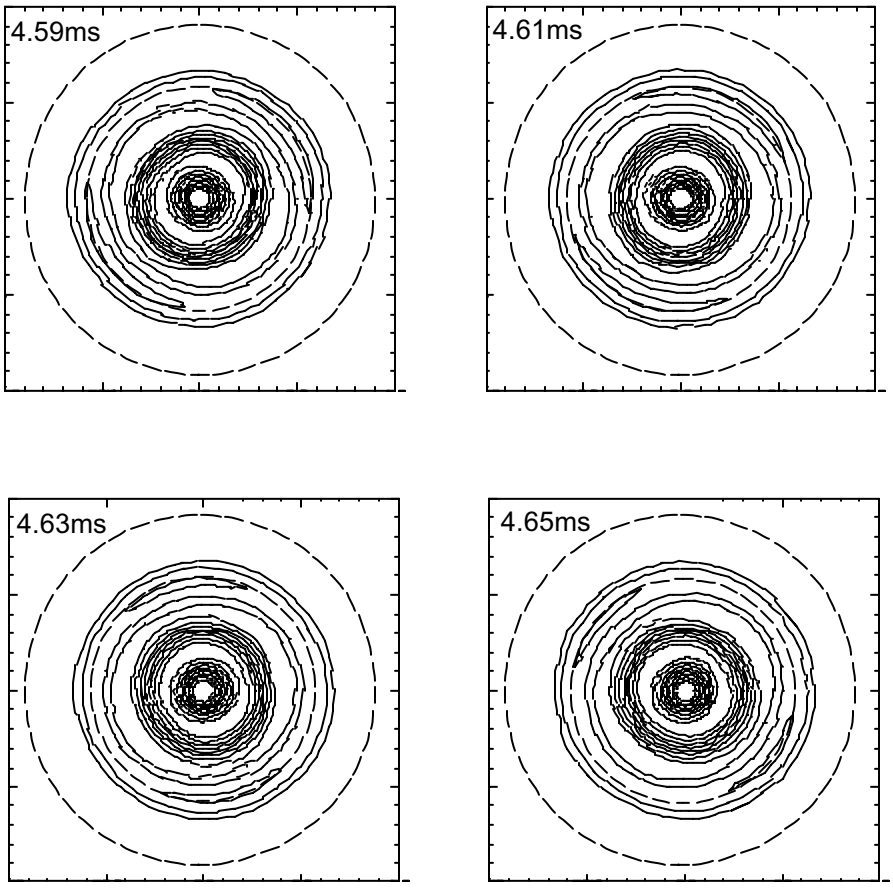

Fig. 7.5 Tomography reconstruction shows m = 2 island structures

Assume the mode has a structure of m = 2 and n = 1, we can map diagnostics at different toroidal location to the same toroidal plane. Fig 7.6 shows the saddle coils, soft X-ray tomography and shell mounted probes on the same toroidal plane. We can then compare the phases of different diagnostics.

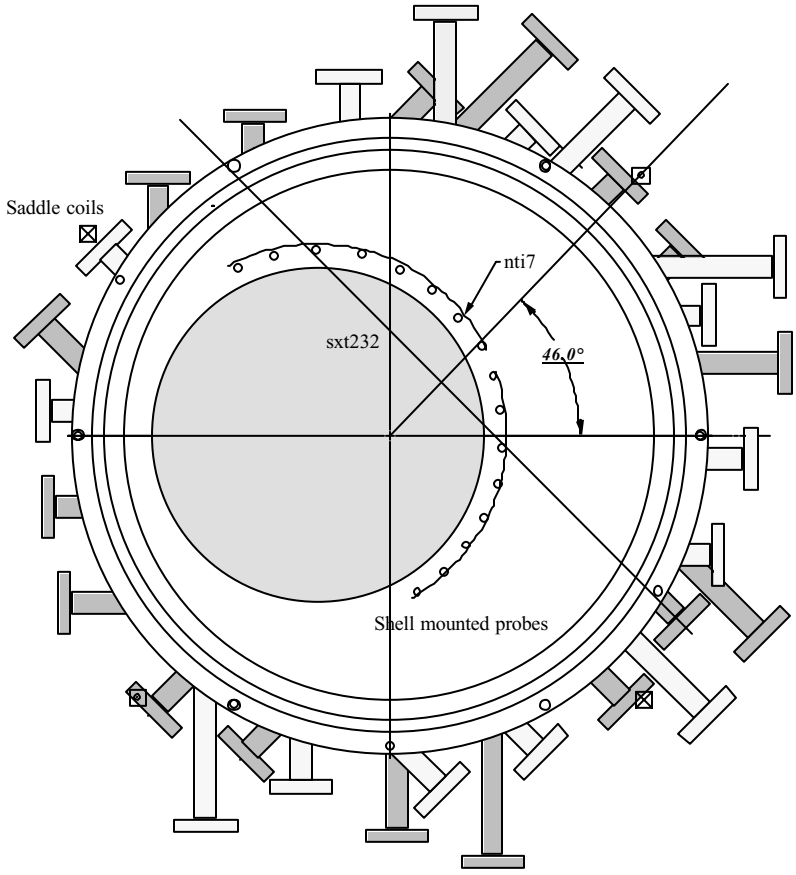

Fig. 7.6 Soft X-ray tomography, shell mounted probes and saddle coils mapped on the same poloidal plane

Figure 7.7 shows the outputs of one of the shell mounted probes and one of the soft X-ray signals. The shell mounted probe locates at approximately 50 degree poloidally after mapping onto the soft X-ray tomography plane assuming the magnetic helicity is m=2/n=1. And the viewing angle of the soft X-ray channel is about 45 degree

poloidally(see fig. 7.6). As we can see, the soft X-ray signal and the shell mounted probe signal has a phase difference about 180 degrees.

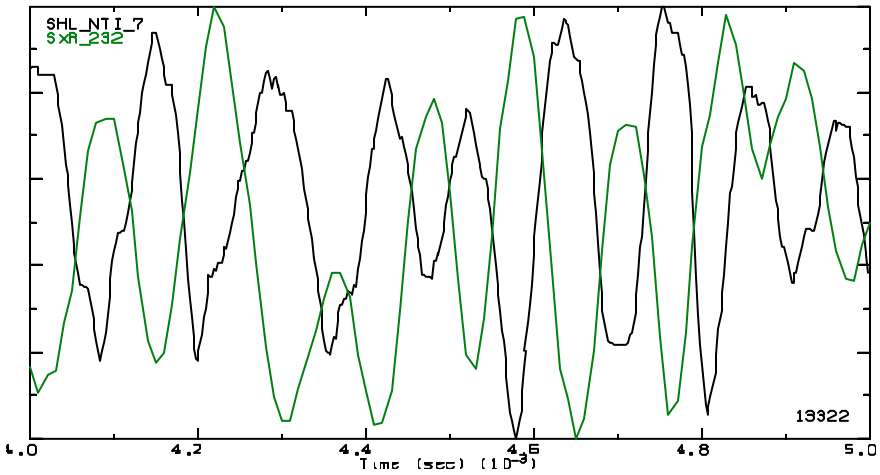

Fig. 7.7 Shell mounted probe signal and soft X-ray signals

7.2 Rotation control with single-phase saddle coils

MHD mode structures have been measured during the applied resonant magnetic field experiments. Mode rotation control using single phase saddle coil set is described in this section. Results using two phase saddle coil set is described in section 7.3.

7.2.1 Description of the experiment

The indication that disruptions with slowly growing precursors may occur in plasmas formed with the shells positioned close to the plasma points to the necessity of providing an active means of suppressing the growth of residual instabilities in wall-stabilized discharges. The approach taken in HBT-EP utilizes the application of

oscillating magnetic perturbations for mode rotation control. This is accomplished using the high-power amplifiers with the modular saddle coil set described in chapter 3. One way of doing the experiment is to connect all the available saddle coils in series, and power them by a single amplifier. The saddle coils are positioned in such a way that the dominant component of the oscillating filed is m/n = 2/1 radial field. In the lab frame, a standing wave is created. Since the plasma has a natural rotating frequency, the magnetic field generated by the saddle coils can be decomposed into two waves traveling in two opposite directions in the plasma frame.

7.2.1 Rotation Control and Mode Structure Measurement

Figure 7.7 shows two plasmas formed with the shells completely inserted which exhibited m/n = 2/1 fluctuations of nearly constant amplitude.

In Fig 7.7, the top two traces are the plasma currents. The second two traces are the current in the saddle coils. The third two traces are output from the Mirnov coils that locate outside the plasma. Also shown here are the moving FFT of the Mirnov signals. In the first discharge, a 350A oscillating current was applied to the saddle coils at t = 1.5 ms. The frequency of the applied field was ramped linearly from 4 kHz to 12 kHz over a period of 3 ms. The pre-existing plasma fluctuations decelerated, locked to the applied perturbation, and accelerated with the applied field over the frequency range f_{MHD} = 5-12 kHz. After the applied perturbation was removed, the plasma mode relaxed to the natural rotation frequency of f_{MHD} = 8 kHz in a time $\tau_M = 500\ \mu s$. Controlled deceleration of instabilities was carried out over the same frequency range in similar discharges. The traces on the left in figure 7.7 show such a discharge.

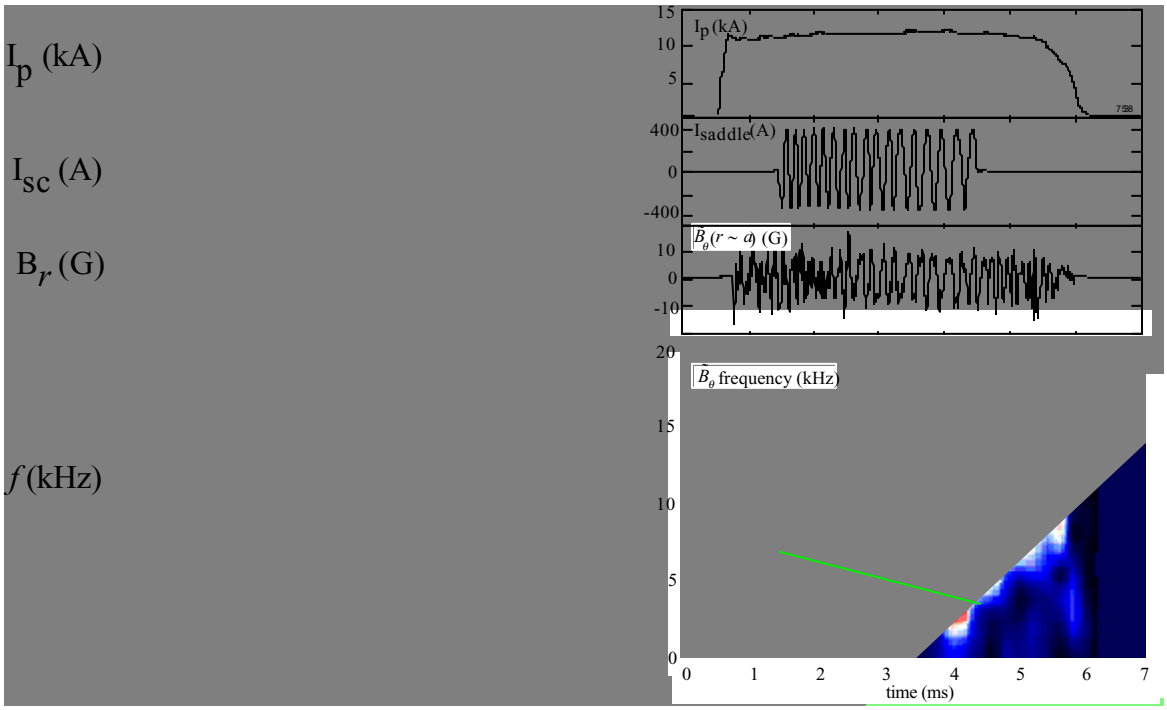

Fig. 7.7 Controlled acceleration and deceleration of slowly-growing instabilities produces factor-of-two changes in mode frequency

It was found that phase difference between MHD mode seen by shell mounted probes and soft X-ray tomography system does not depend on the frequency of the mode. Figure 7.8 and figure 7.9 illustrate this result. When the saddle coil current is on, the frequency increases as in figure 7.8 and decreases as in figure 7.9 while the differences of the mode phase seen by shell mounted probes and soft -X ray tomography system are flat. In comparison, figure 7.9 shows the evolution of phase difference seen by the two diagnostics in a discharge with the saddle current off.

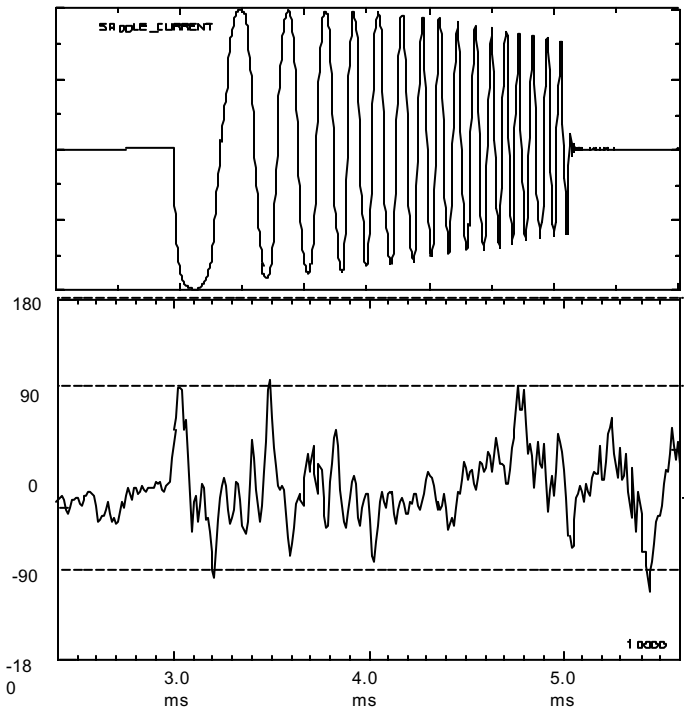

Fig. 7.9 Frequency ramp down. Phase difference between mode seen by shell mounted probes and soft X-ray tomography system

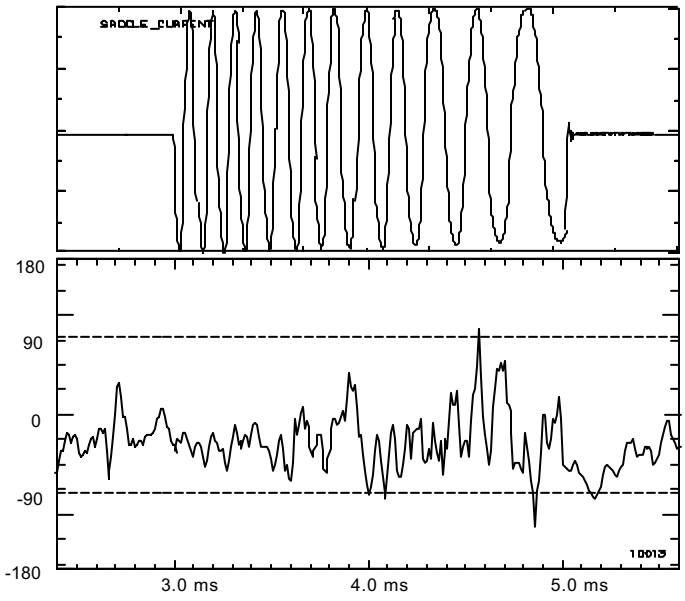

Fig. 7.10 Frequency ramp-up. Phase difference between mode seen by shell mounted probes and soft X-ray tomography system

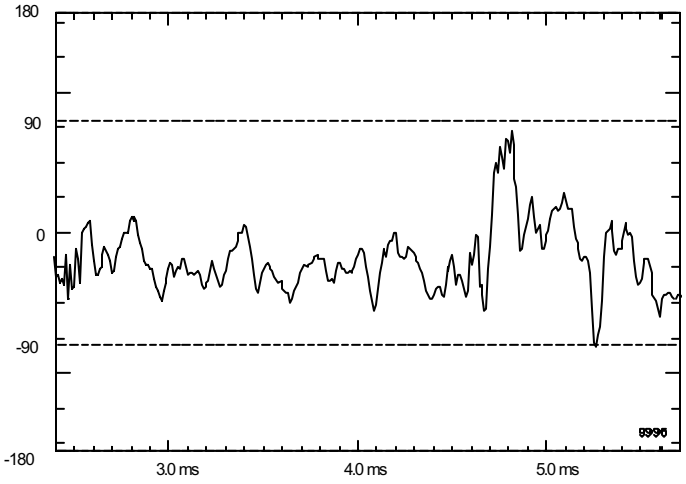

Fig. 7.11 Saddle coil off. Phase difference between mode seen by shell mounted probes and soft X-ray tomography system

Figure 7.12 shows the phase and frequency evolution of the m = 2 magnetic signal. Before the saddle coil was turned on, the plasma rotates smoothly as seen on the phase difference between the applied magnetic field and the plasma response. When the frequency of the saddle coil is smaller than the plasma natural frequency, the phase of the plasma lags the saddle current phase. When the saddle current frequency is larger than the plasma natural frequency, the phase of the plasma rotation leads the saddle current phase. The plasma frequency has a trend of increasing with the applied saddle current frequency. However, the plasma rotation frequency has large modulation around the saddle current frequency.

Figure 7.12 Single-Phase Rotation Control with Five Saddle-coil pairs

The previous experiment was carried out using 5 saddle coils connected in series. Experiments were also carried out on HBT-EP using only two saddle coils. It was found that even with only two saddle coils, the applied resonant magnetic field can still modify the MHD mode rotation speed. Figure 7.8 shows a discharge in which only two saddle coils were used to modify the rotation profile. The mode rotates with greater jitters. And when the frequency of the saddle current is large, the mode fails to lock to the applied field.

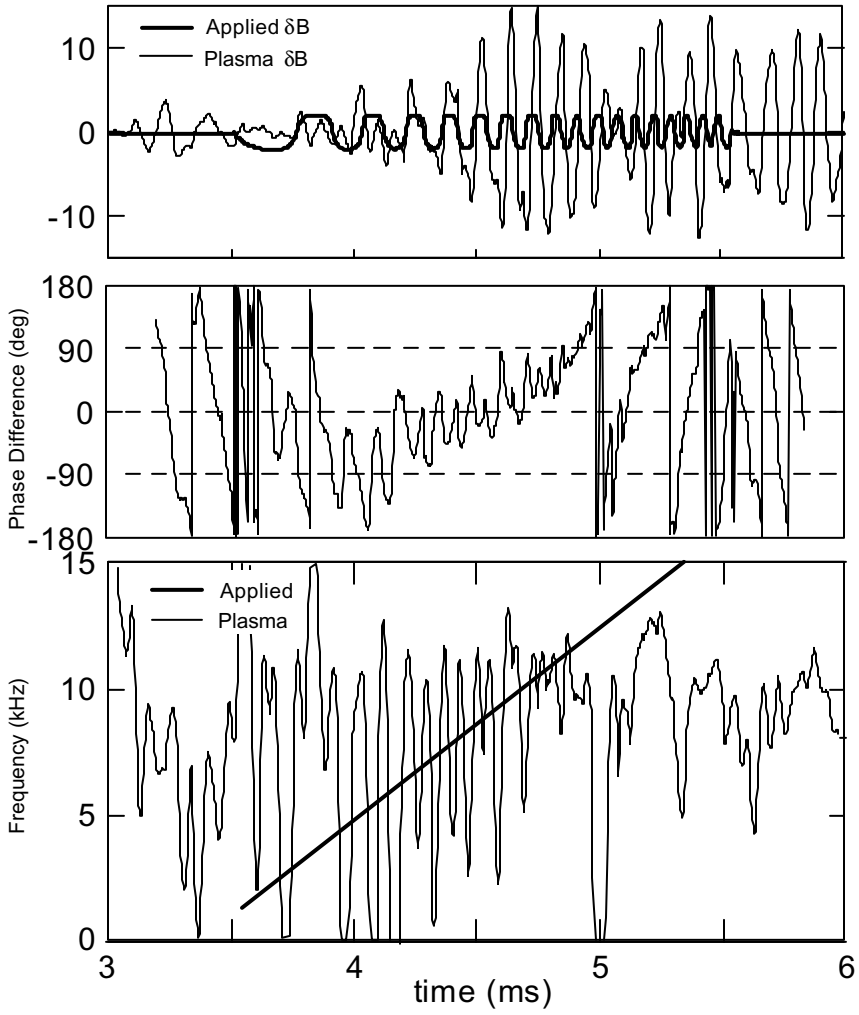

Figure 7.13 Single-Phase Rotation Control with Two Saddle-coil pairs

Figure 7.14 shows the perturbations of the soft X-ray signals from the detectors that locate at the r = 10 cm but different poloidal angles. The analysis method is the same as the one in Figure 7.3. The equilibrium parts of the signals have been stripped off. What's shown here is the perturbation component of the soft X-ray signals. The color indicates the amplitude of the perturbation, with red means positive and blue means negative. The slope of the stripes indicates the plasma rotation frequency.

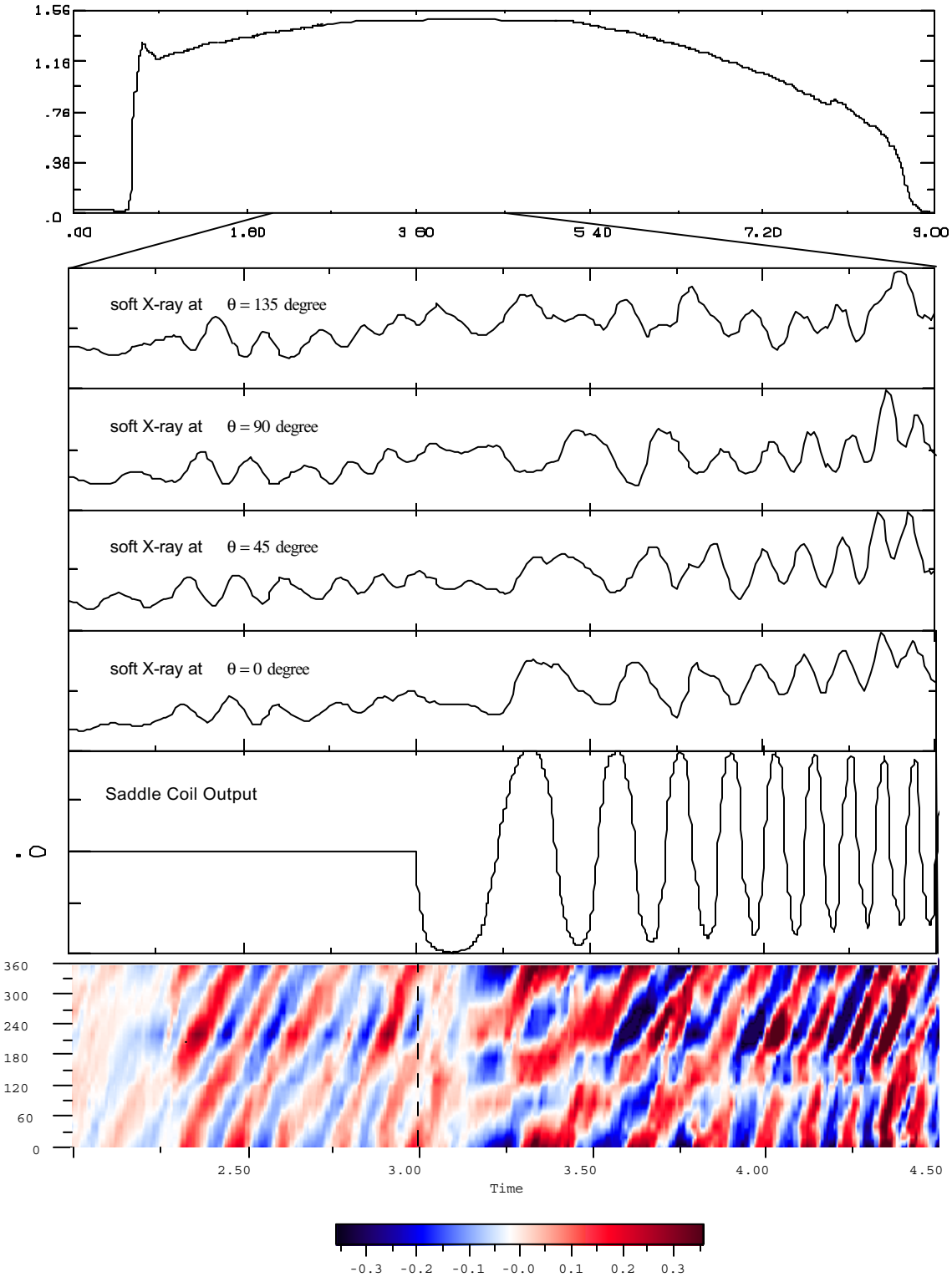

Fig. 7.14 MHD mode structure seen by soft X-ray tomography system in single phase, five saddle coil mode rotation control experiment

By counting the number of peaks at a particular time, we can tell the dominant mode number is m = 2. Also shown here are the signals from four of the eight channels that locate at 0^0, 45^0, 90^0 and 135^0. As we can see from the graph, the plasma rotates with a relatively constant frequency before the saddle coils are turned on. When the saddle coil current is on, the mode locks to the saddle coil frequency which is smaller than the natural frequency. As the frequency of the saddle coil current increases, the mode rotation frequency increases. This is a definitive proof that we have successfully rotated the MHD mode.

Fig 7.15 is a tomographic reconstruction at 4.15 ms for the same shot. The same algorithm as the one used in Fig. 7.5 was used here. Again the reconstruction shows m = 2 island structure.

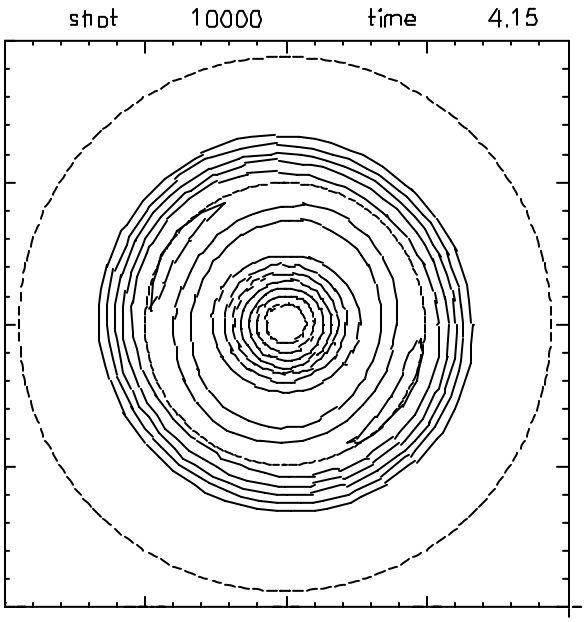

Fig. 7.15 tomographic reconstruction at 4.15 ms

7.2.3 Comparison with Theory

Chapter 2 described a model for the evolution of the amplitude and phase of an MHD mode. The oscillating magnetic field exerted by the saddle coil current and eddy current in the conducting shells determine the dynamics of the amplitude and phase of the MHD mode. The governing equations are:

$$\frac{db}{dt} = g_1(1-\sqrt{b})\sqrt{b} + g_2\frac{b_d}{\sqrt{b}}, \tag{2.7}$$

and

$$\frac{d\varpi}{dt} = h_1 b b_q - h_2 b^2\left(\frac{\varpi\tau_w}{m^2+\varpi^2\tau^2}\right) - h_3(\varpi-1). \tag{2.8}$$

in which

b = Normalized perturbed radial field,

g_1 = Rutherford island growth rate,

g_2, h_1 = Forces from coils,

ω = Normalized mode rotation rate,

and

h_3 = Plasma viscosity.

Figure 7.16 shows the result of simulation using the model described. The phase of the MHD mode increases from lagging the phase of saddle current to leading it as the

frequency of the applied saddle coil current increases. The frequency of the MHD mode increases as the saddle current frequency increases. The frequency of the MHD mode presents large modulations. This result is consistent with the experimental observations above.

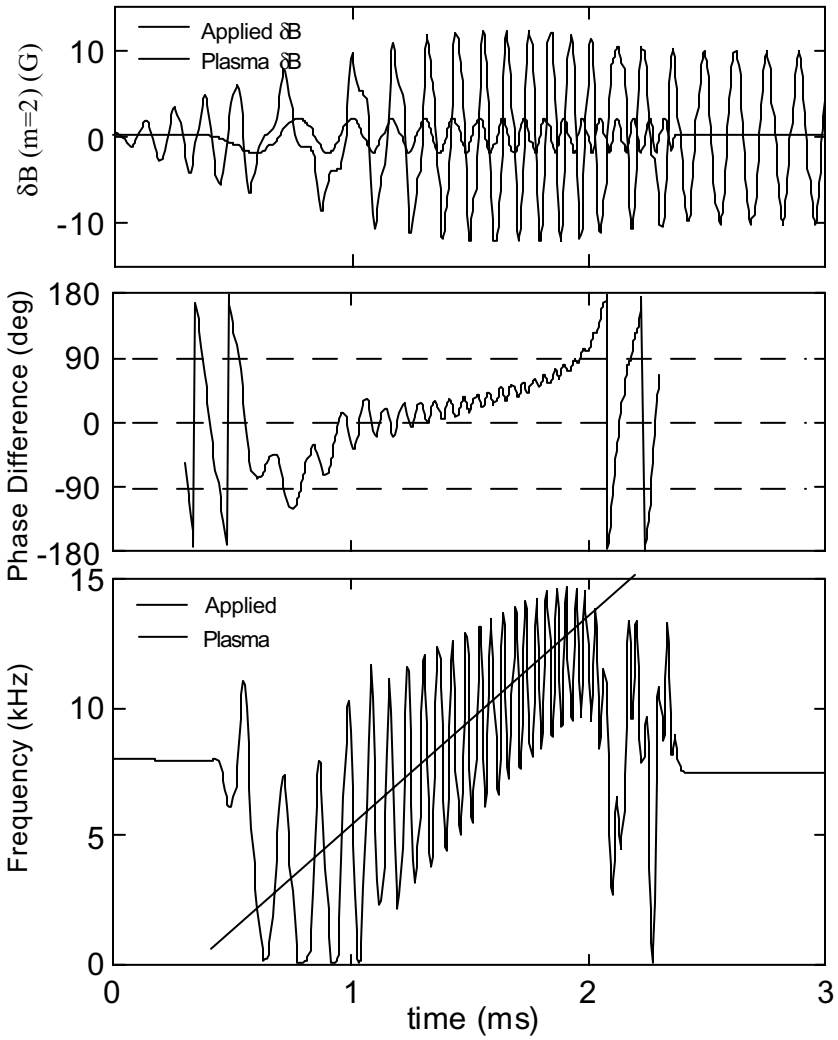

Fig. 7.16 Single-helicity tearing-mode dynamic simulation

7.3 Rotation Control with Two-phase Saddle Coils

Another way of doing the experiment is to power the available saddle coils by two sets of amplifiers. The dominant component of the oscillating filed created by the saddle coils is m/n = 2/1 radial field. The oscillating magnetic field created by the two saddle coils have a phase difference of 90^0. So a traveling wave with m = 2 structure is created in the plasma.

Figure 7.17 shows a discharge of two-phase mode rotation control using two sets of saddle-coil pairs. Between 3.5 ms and 5.5 ms, the frequency of the saddle coil current is ramped from 2 kHz to 13 kHz. The natural mode rotation frequency is about 8.5 kHz for this discharge. The phase difference between the MHD mode presents similar result as in the single phase case. Between 2.5 ms and 4.3 ms, the saddle coil current frequency is less than the natural mode rotation frequency. We can see from Figure 7.10 that the phase of the applied field is less than the mode rotation frequency, and the phase difference increases from -90^0 to 0^0. The applied resonant magnetic field drags the rotating mode and slows it down. When the frequency of the applied field is above the natural mode frequecy, the phase of the applied field starts to lead the mode rotation frequency. This indicates that the applied resonant magnetic field pulls on the rotating mode and speeds it up.

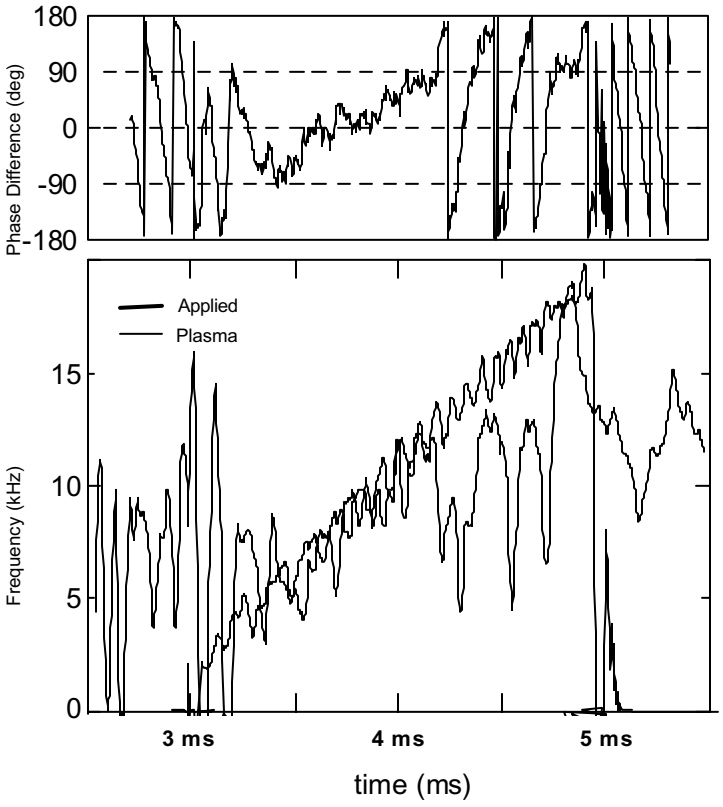

Fig. 7.17 Two-phase mode rotation control using two sets of saddle-coil pairs

The frequency of the MHD mode also increases as the applied saddle current frequency increases. However, the modulations in the frequency of the MHD mode is smaller than the single phase case.

Figure 7.18 shows the phase evolution seen by the soft X-ray tomography system in a double phase rotation control discharge. Before the saddle coil was turned on, the phase evolves smoothly in natural frequency. After the saddle coil current was turned on, the phase evolves in the frequnecy of the saddle current, and it shows jitters.

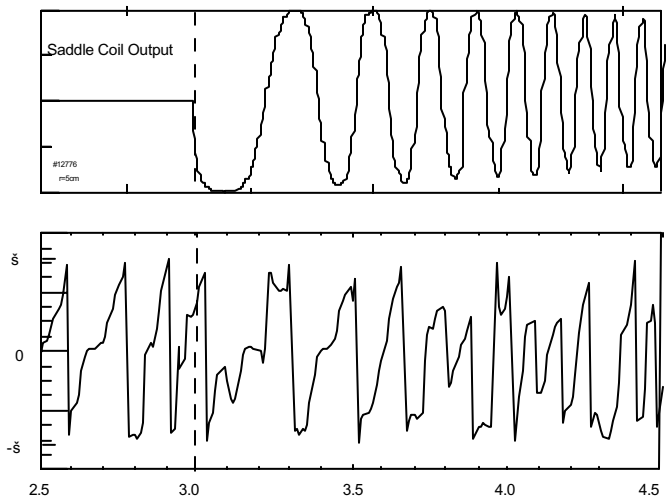

Fig. 7.18 Phase evolution in double phase rotation control

Figure 7.19 shows the multiple-phase nonlinear simulation with rotating magnetic perturbation. Comparing with single-phase simulation, the frequency exhibits much less

jitters. This indicates that it's easier for the MHD mode to lock to the applied magnetic field.

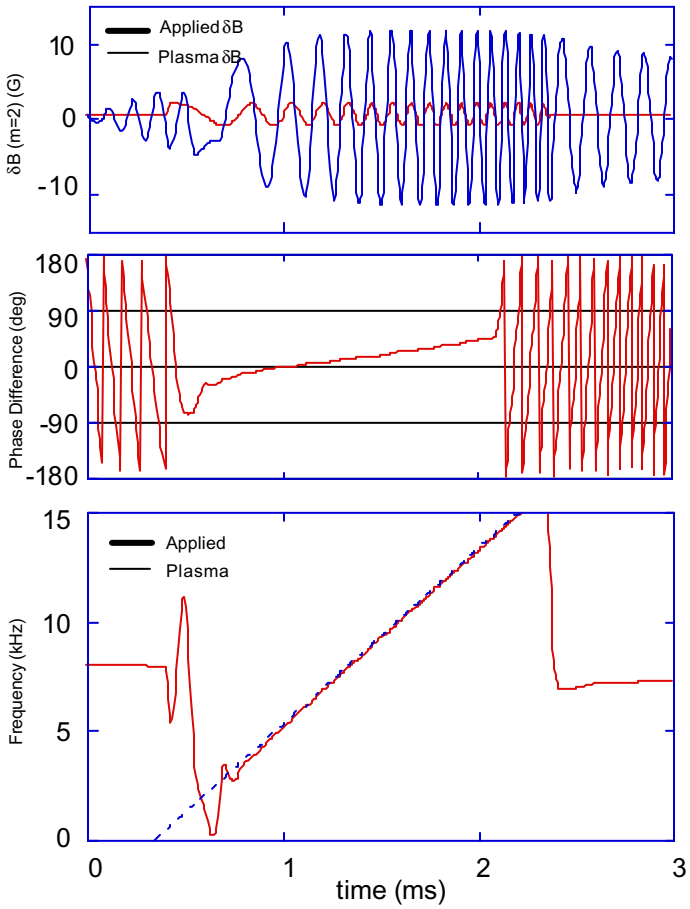

Fig. 7.19 Multiple-phase nonlinear simulation with rotating magnetic perturbation

References

[1] T.H. Ivers et al., Plasma Physics and Controlled Nuclear Fusion Research **1994** IAEA, Seville (1994).

[2] D. Gates, Ph.D. thesis, Columbia University, 1993.

[3] R. Kombargi, Ph.D. thesis, Columbia University, 1997.

[4] A. Garofalo, Ph.D. thesis, Columbia University, 1997.

[5] N. Eisner, Ph.D. thesis, Columbia University, 1997.

[6] J.C. Hosea, et al., in Plasma Physics and Controlled Nuclear Fusion Research, Madison, 1970(International Atomic Energy Agency, Vienna, 1971), Vol. 1, p. 573

Chapter 8

Conclusion

8.1 Summary of the results

A soft X-ray tomography system has been built to measure MHD mode structures. Soft X-ray radiation from plasma is approximately proportional to $n_e T_e$. MHD instabilities cause soft X-ray radiation signal to fluctuate. The structure of the oscillating component of soft X-ray provides MHD mode structure information.

A vacuum chamber section with 32 viewing ports was built. One soft X-ray sensitive photodiode is mounted on each port.. The photodiodes are coated with a specially designed thin film filter consisting of 100nm Zr, 7.5nm Ti and 75nm C. Signals from the 32 photodiodes are inverted by reconstruction programs to give the 2 dimensional profile of the soft X-ray radiation from the plasma. This diagnostic together with the magnetic probes provides information of the MHD mode structures on HBT-EP.

Plasma discharges that are kink-mode stabilized by the conducting walls are prepared for the experiments. Oscillating components of the soft X-ray signals of the detector channels located at the same radial position but different poloidal positions show a dominant poloidal mode number of m = 2. Soft X-ray radiation tomography reconstructions show m = 2 island structures which indicates that it is tearing mode.

Phases of soft X-ray signals are also compared with the phases of magnetic signals from the shell mounted probes. After mapped the two diagnostics on the same

toroidal plane, a soft X-ray signal located at r = 10 cm and $\theta = 50$ degrees and a shell mounted probe signal that located $\theta = 45$ at show a phase difference of approximately 180 degrees. The phase difference between the mode structure seen by soft X-ray tomography system and the mode structure seen by the shell mounted probes is a constant as a function of time.

Extensive studies of the mode structure of m = 2 MHD instabilities have been carried during the applied resonant magnetic field experiments on the HBT-EP tokamak.

A set of modular saddle coils producing m/n = 2/1 radial magnetic field has been installed on the HBT-EP. The saddle coils are located at the quartz segments to allow field penetration. They were driven by power amplifiers provided by the Los Alamos National Lab. By selecting the oscillating current in the saddle coils, the frequency and amplitude of the applied resonant magnetic field can be programmed.

Experiments demonstrated that applied oscillating resonant magnetic fields with both single-phase and two-phase are capable of modulating the MHD mode rotation. Controlled acceleration and deceleration have been observed by programming frequency of the applied saddle coil current. The phase difference between the mode structure seen by soft X-ray tomography system and the mode structure seen by the shell mounted probes is a constant as a function of time in both the controlled acceleration and deceleration discharges.

The perturbations of the soft X-ray signals from the detectors located at the same radial position but different poloidal angles clearly show we successfully controlled the rotation of m = 2 mode. Tomographic reconstruction also identifies this mode has m = 2 island structure.

Two-phase applied perturbations induced less instantaneous modulation of the mode rotation.

A model taking into consideration the torque exchange between the applied perturbations and the rotating plasma at the resonant magnetic surface has been used to explain the rotation control by applied resonant magnetic field. The theoretical results and the experimental results fit to each other qualitatively.

8.2 Suggestions for future work

The MHD mode structure information obtained by the soft X-ray tomography system and the other diagnostics can be used in the feedback control study of MHD modes.

A Digital Signal Processor (DSP) feedback controller system has been developed to study the active feedback control of the MHD instabilities. We can use both the soft X-ray tomography signals and the magnetic signals as the inputs to the feedback system to create a programmable, digital control loop. The soft X-ray signals are particularly useful since they provide the internal and more localized information about MHD mode structures.

Applied resonant magnetic field has been demonstrated to be able to change the rotation of the MHD modes. However, the relationship between the MHD mode rotation and the plasma bulk rotation cannot be studied by the currently available diagnostics. The issue whether applied resonant magnetic field can change the bulk plasma rotation profile still exists. The study of the rotation profile of the bulk plasma is important, since

theoretical results suggest that special plasma rotation speed and profile can suppress certain forms of turbulence and make the plasma discharge insensitive to error fields.

Two additional diagnostics have been developed to measure the plasma flow on HBT-EP. A wavelength scanning monochrometer views the Doppler shift of various impurity lines due to toroidal plasma flow. The monochrometer views two opposite toroidal directions simultaneously. The use of two views allows the calculation of the Doppler shift without an absolute wavelength calibration. The monochrometer sits on a translation table, which allows the viewing of different tangency radii in the plasma.

A movable double/Mach probe has also been in development on HBT-EP to measure the plasma flow shear at the edge. The probe can be inserted into the edge of the plasma without degrading the overall experimental performance.